SINGLE-EVENT MECHANISMS IN InAlSb/InAs/AlGaSb HIGH ELECTRON MOBILITY TRANSISTORS

By

Vishwanath Ramachandran

Dissertation
Submitted to the Faculty of the
Graduate School of Vanderbilt University
in partial fulfillment of the requirements
for the degree of

DOCTOR OF PHILOSOPHY

in

Electrical Engineering

May 2013

Nashville, Tennessee

Approved:

Professor Robert A. Reed
Professor Ronald D. Schrimpf
Professor Michael L. Alles
Professor Arthur F. Witulski
Professor D. Greg Walker

ACKNOWLEDGMENT

Mark Twain, my favorite humorist of all time, said this about discovery in his 1906 comic short story, *Eve's Diary*, "If there wasn't anything to find out, it would be dull. Even trying to find out and not finding out is just as interesting as trying to find out and finding out; and I don't know but more so." I think Graduate School allows one to experience the "joy of discovery", through research, and boy, is there ever a dull moment!

There have been a number of people who have helped me in my course of discovery here at Vanderbilt, starting with my Masters', and through my Ph. D. research that I would like to acknowledge. My Ph. D. committee members were immensely helpful during every step of the way, with their valuable inputs and advice. My Advisor, Dr. Robert Reed, and Dr. Ron Schrimpf, have not just been members on the committee but have been my research mentors throughout the course of my time at Vanderbilt. As the PI of the Vanderbilt contingent, Dr. Mike Alles gave me the opportunity to work on the multi-University, multi-Industry NASA SiGe project that provided me with valuable technical and practical experience. Dr. Dan Fleetwood, along with Dr. Ron Schrimpf, gave me my first break at Vandy through the LDO project that eventually led to my Masters' Thesis. Dale McMorrow and Brad Boos from Naval Research Labs provided all devices used for colleting data in this dissertation, and also helped with data collection and technical discussions. Xiao Shen and Dr. Sokrates Pantelides have partaken in useful technical discussions that aided simulation analyses carried out in this work.

Mike McCurdy deserves a special mention for being a pillar of support during my early single-event testing days. Andrew Sternberg, Kevin Warren, and Marcus Mendenhall

have all chipped in during various stages of this work. John Fellenstein and Bob Patchin from the workshop have been immensely helpful in fabricating customized contraptions used heavily in this work. Fellow RER friends Nick Pate, Nick Hooten, Mike King, Jonny Pellish, and Enxia Zhang have all chimed in at one time or another, be it helping carrying out tests, assembling packages, or proof-reading. Michele Cedzich made sure that all of the innumerable but somehow urgent administrative requests were always addressed on time. Last but not the least, I thank DTRA and NASA for funding the projects I have been involved in, without which this work would not have been possible.

To my parents and family, who have been a strong and encouraging presence in spirit throughout the course of my Vanderbilt career, I dedicate this dissertation to them.

TABLE OF CONTENTS

Page

LIST OF FIGURES

Figure Page

CHAPTER I

INTRODUCTION

A. Background

Antimonide-based compounds such as AlSb, GaSb, and InSb, along with their ternary and quaternary alloys, are ideally suited for use in high electron mobility transistors (HEMTs) in low-power, radio frequency (RF) applications. This is primarily because of the excellent transport properties of the antimonide-based compound semiconductors (ABCS) materials that lend themselves to increasing frequencies (lower wavelengths) of operation at relatively lower power consumption when compared to silicon, germanium, and other III-V materials [1]. The ABCS materials have lattice constants greater than 6.0 Å as shown in Fig. 1, and lattice-match well with other materials from the same family [1]. The ABCS materials restrict themselves to low-power operation by the use of low (room temperature) bandgap channel materials (for e.g. InAs – 0.36 eV, and InSb – 0.17 eV), and thus are ideal for low-power operation.

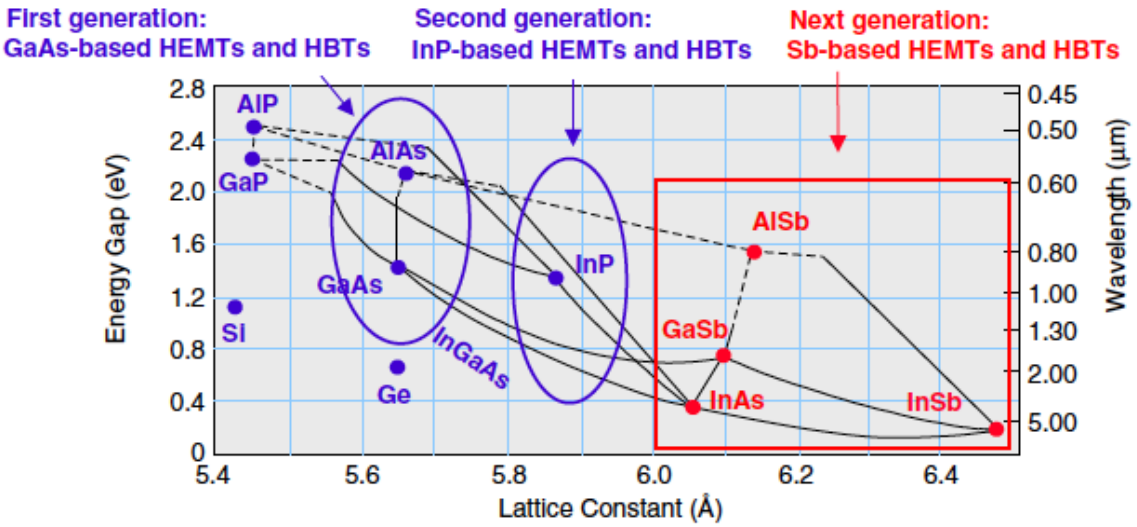

Fig. 1. Evolution of the trend towards use of larger lattice constants and smaller bandgap ABCS materials for high-speed, low-power HEMTs. After [1].

In particular, ABCS HEMTs with InAs channels exhibit relatively high channel carrier concentrations and high room temperature low-field electron mobilities, velocities, and two dimensional electron gas (2DEG) sheet charge densities, typically 25,000 cm^2/V-s, 2×10^7 cm/s, and $8 \times 10^{12}/cm^2$, respectively [2]. High carrier confinement is possible because of the large conduction band offsets (ΔE_C) between InAs and the barrier materials such as $In_{0.2}$ $Al_{0.8}Sb$ (ΔE_C = 1.1 eV) or AlSb (ΔE_C = 1.35 eV), the latter shown in Fig. 1. These excellent electrical characteristics make ABCS HEMTs attractive candidates for use in space technologies.

B. Motivation and scope of work

Two main variants of ABCS HEMTs include AlSb/InAs/AlSb and InAlSb/InAs/AlGaSb HEMTs. The former has been around for several decades with pioneering work done by Herbert Kroemer and his group at UCSB [3-5], and has been the subject of extensive research from electrical, material, and reliability perspectives. On the other hand, InAlSb/InAs/AlGaSb HEMTs have been processed relatively recently by researchers at Naval Research Labs (NRL) [6]. Barring a few material-based studies on these HEMTs [7, 8], relatively little is known about these devices.

Research into proton-induced total ionizing dose effects on AlSb/InAs/AlSb HEMTs show that radiation-induced drain current decrease is significantly less than their AlGaAs/GaAs metal semiconductor field effect transistor (MESFET) counterparts [9]. A similar effect has been observed in InAlSb/InAs/AlGaSb HEMTs [10]. While single-event effects research have been carried out on AlSb/InAs/AlSb HEMTs through experiments [11,12] and modeling [13], corresponding research on InAlSb/InAs/AlGaSb

HEMTs is very limited [14]. Being relatively recent, the processing technologies of InAlSb/InAs/AlGaSb HEMTs continue to evolve, and are not as mature as those existing in silicon complementary metal oxide semiconductor (CMOS) devices. As a consequence, the unintended variations in the InAlSb/InAs/AlGaSb device structure can be relatively large. These include variations in the barrier and channel thickness, delta-doping, and unintentional buffer doping across devices on the same wafer. All of these translate into threshold voltage (V_T) variations that affect the 2-dimensional electron gas (2DEG) density in the channel, and thus the current drive, for a given gate bias. Therefore, V_T variation effects need to be accounted for in order to make a meaningful interpretation of the experimental single-event data in InAlSb/InAs/AlGaSb HEMTs.

This research identifies and studies single-event mechanisms in InAlSb/InAs/AlGaSb HEMTs in detail. It characterizes single-event transients in InAlSb/InAs/AlGaSb HEMTs using broadbeam and microbeam heavy ion experiments along with 2-D technology computer-aided design (TCAD) modeling. The broadbeam experiments show that single-event cross-sections can be large enough to encompass not only the channel but also the drain-source alloy and buffer interfaces. Corresponding 2-D TCAD modeling reveal that it is possible to generate single-event transients from an imperfect drain alloy-buffer interface. Microbeam experiments are used to validate the TCAD modeling results and additionally show that the channel region is the most sensitive to single-event effects. This research studies the single-event transient sensitivity to gate bias through additional broadbeam heavy ion experiments and shows that the integrated charge reaches a maximum at threshold bias and drops off at both depletion and accumulation biases. Additionally, this work incorporates 2-D TCAD modeling to study the effect of changes

in device features such as delta-doping, channel thickness, and barrier thickness on the corresponding single-event response. Finally, this dissertation reports on the potential influence of defects in the AlGaSb buffer and InAlSb barrier on the corresponding single-event response through 2-D TCAD simulations. These types of analyses serve as a useful aid in the technology development of ABCS HEMTs.

C. Organization of the dissertation

Chapter II gives an overview of ABCS HEMTs with InAs channels and the basics of their operation. Chapter III describes the InAlSb/InAs/AlGaSb HEMT, and presents an overview of previous single-event research carried out on III-V HEMTs. Chapter IV presents the first set of single-event experiments carried out on the InAlSb/InAs/AlGaSb HEMTs using broadbeam heavy ion and microbeam experiments along with 2-D TCAD modeling to identify the mechanisms of single-event-induced current transients in InAlSb/InAs/AlGaSb HEMTs. Chapter V details the set of broadbeam experiments carried out on InAlSb/InAs/AlGaSb HEMTs to investigate the gate bias sensitivity to single-event transients. The outcomes of these experiments are analyzed through 2-D TCAD modeling and the device mechanisms responsible for the observed single-event responses are determined. Chapter VI carries out a 2-D TCAD modeling-based analysis of the single-event response sensitivity of the InAlSb/InAs/AlGaSb HEMT to changes in device features such as buffer and delta-doping, and barrier and channel thicknesses. The effects of traps in the AlGaSb buffer on the corresponding single-event response are also examined using simulations. Chapter VII summarizes the work and highlights potential scope for future work on InAlSb/InAs/AlGaSb HEMTs.

CHAPTER II

INDIUM ARSENIDE AND ABCS HEMTS

A. InAs superiority

Indium arsenide is an attractive material for use in low-power, high-frequency ABCS HEMTs. In AlSb/InAs/AlSb HEMTs, for example, the high conduction band offset (ΔE_C = 1.35 eV) and the best lattice matching (lattice constant a = 6.058 Å and 6.136 Å for InAs and AlSb, respectively) among the III-V family ensure strong electron confinement in the InAs quantum well with a very high tunneling barrier. This is depicted in Fig. 2. For $In_{0.2}Al_{0.8}Sb$ barriers in InAlSb/InAs/AlGaSb HEMTs, the ΔE_C changes slightly to 1.1 eV but is still deep enough for strong electron confinement, as shown in the band diagram of Fig. 3. Additionally, the high value of ΔE_C ensures that the donor electrons from the modulation doping in the $In_{0.2}Al_{0.8}Sb$ are attracted towards the InAs channel. This keeps the conduction band of the InAs channel populated by electrons even at zero bias, thereby resulting in a depletion-mode device as seen in Fig. 3. The large value of ΔE_C also prevents any dramatic shift in the Fermi level at low temperatures since it is energetically unfavorable for the electrons to move out of the channel at those temperatures. Consequently, incomplete ionization or “freeze-out” of the channel carriers does not occur at very low temperatures - a very distinct advantage over silicon devices for low temperature applications.

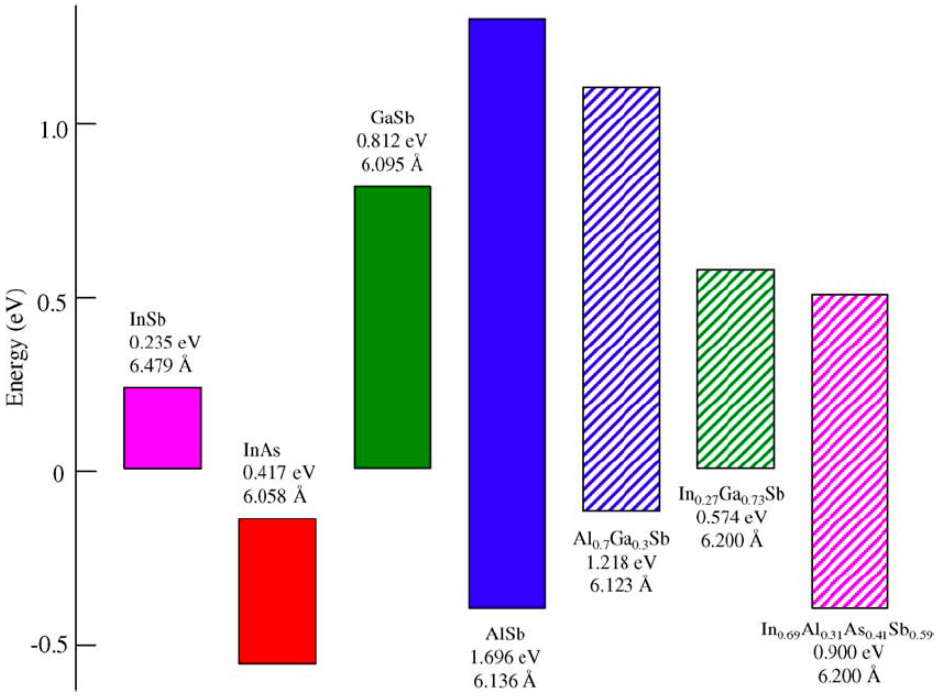

Fig. 2 Band alignments for ABCS alloys at 0K. After [1].

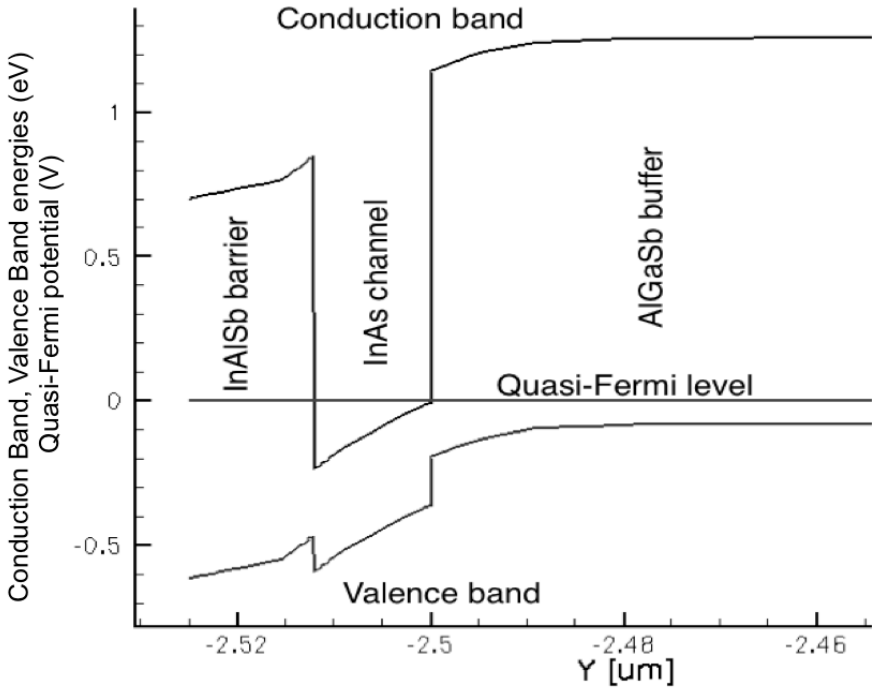

Fig. 3. Band diagram of the InAlSb/InAs/AlGaSb HEMT obtained from a simulator, through a vertical cutline passing through the center of the gate.

Also, the lower effective mass of electrons in InAs (m_e of InAs = $0.023m_o$, where m_o is the electron rest mass) in the Γ valley compared to all other III-V materials (except InSb) translates into high electron mobilities and saturation velocities in the InAs channel. These not only reduce device transit times, but also result in low parasitic resistances. Consequently, one gets very high room-temperature low-field mobilities and 2DEG densities, with low-field mobility of 980,000 cm^2/V-s at a 2DEG density of 1.65×10^{12} cm^{-2} being reported at 4.2K [15].

In III-V HEMTs, the doping is done differently with respect to traditional silicon devices. In a typical silicon device, the bulk (substrate) doping directly influences the inversion layer formation and the corresponding device threshold characteristics. In other words, there is no spatial separation between the dopant atoms (in the bulk) and the channel electrons. This gives rise to ionized impurity (dopant) scattering between the channel electrons and the dopants, and leads to undesired effects such as channel low-field mobility decrease, thereby directly affecting the current drive. In a III-V device such as the InAlSb/InAs/AlGaSb HEMT, a thin layer (usually 10-20 Å) of dopant atoms (usually tellurium) is deposited in the (InAlSb) barrier layer on top of the channel layer at a specific temperature to reduce scattering of the tellurium in the barrier layer. Due to the large conduction band offset between the barrier and the channel conduction band seen in Fig. 3, the electrons from the tellurium dopant atoms fall into the deep channel (quantum well) thereby populating the channel with electrons for conduction. This type of doping employed in III-V HEMTs is called modulation doping.

Thus there is a distinct, spatial separation between the dopant atoms in the barrier, and the conduction electrons in the channel. This obviates the problem of ionized impurity

scattering affecting the mobility of the conduction electrons in the channel thereby enabling the InAlSb/InAs/AlGaSb HEMTs to have high channel mobilities as described in the previous section. Moreover, the channel quantum well structure ensures that the energy levels are distinct and quantized. Owing to this quantization, the channel electrons are "fixed" in position in the direction parallel to the channel conduction band. These electrons can thus move only in the other two dimensions and are therefore called two-dimensional electron gas or 2DEG. A combination of spatial separation of the channel and dopant atoms and thus the energy quantization levels in the deep InAs well (usually denoted as states E_0 and E_1 with an energy difference of 0.4 eV [15]), along with employment of modulation doping greatly reduces ionized impurity scattering. These result in enhanced room-temperature low-field mobilities. The deep levels mitigate the freeze-out of carriers at low temperatures evidenced in other semiconductors. Consequently, we have high 2DEG densities and mobilities even at low temperatures as reported above.

B. Practical application of ABCS HEMTs

AlSb/InAs/AlSb HEMTs with a gate length of 0.5 μm have been shown to exhibit outstanding transconductance values of 1.1 S/mm, drain saturation currents of 750 mA/mm and gate leakage currents less than 10 nA at low gate bias [16]. The corresponding cut-off frequency (f_T) and maximum oscillation frequency (f_{max}) values were 120 GHz and 100 GHz, respectively. Northrop Grumman has successfully demonstrated the operation of a W-band three-stage InAlSb/InAs/AlGaSb HEMT-based monolithic microwave integrated circuit (MMIC). The MMIC, shown in Fig. 4, has a

remarkable 16 dB gain over the 77-103 GHz frequency band and an ultra-low power dissipation of 0.6 mW per stage, which is just 3% of that of a corresponding GaAs MMIC operating at the same frequency [17]. More recently, Chou and others have demonstrated the use of a 0.1 μm gate length InAlSb/InAs/AlGaSb HEMT MMIC for use in phased array detectors with excellent DC characteristics and an f_T value of 220 GHz [18].

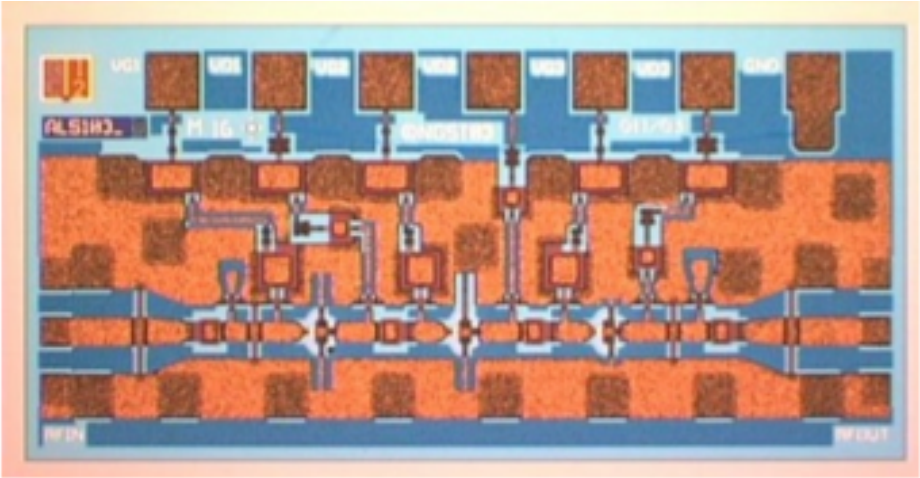

Fig. 4(a). A three-stage AlSb/InAs/AlSb HEMTLNA MMIC. After [17].

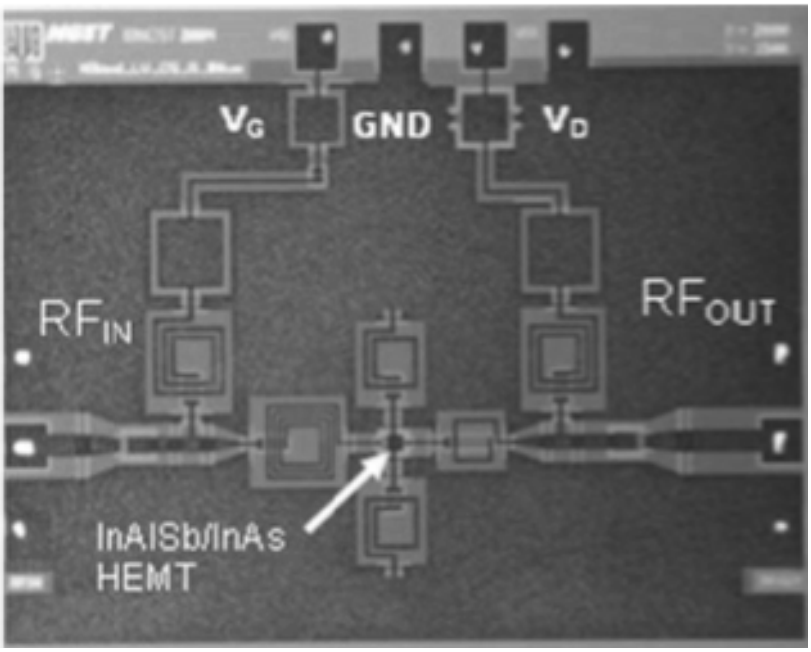

Fig. 4(b). An InAlSb/InAs/AlGaSb HEMT MMIC used in a phase-detector array. After [18].

The AlSb/InAs/AlSb and InAlSb/InAs/AlGaSb HEMT development also receives significant technological support from DARPA and Intel (in partnership with NRL), highlighting the increased research interest in this material system.

C. Introduction to radiation effects

The energetic particles that characterize natural space radiation environment can be classified into two broad categories, viz.: (a) trapped particles in the earth's magnetic field that consist mainly of electrons and low-energy protons and (b) cosmic rays of galactic or solar origin that consist of heavy ions and high-energy protons [19]. The earth's magnetic field traps relatively low-energy particles forming radiation "Van Allen belts" named after Van Allen, who first reported the existence of these trapped energetic particles using detectors aboard a satellite in 1958 [20]. The motion of these trapped charged particles forms bands of electrons and protons around the earth and form the earth's radiation belts. These belts extend from one to fourteen earth radii or R_E, as seen in Fig. 5, which summarizes the distribution of proton flux as a function of energy and R_E. Flux is defined as the rate at which the energetic particles impinge upon a unit surface area, given in units of particles/cm^2-s. The fluxes for the protons and electrons as a function of satellite orbit are calculated by two models, the AP8 [21] and AE8 [22] respectively. Work is currently underway to update the models with corresponding new releases of these models, AP9 and AE9.

The trapped protons primarily extend from slightly above one to 3.8 R_E, with energies greater than 10 MeV [23]. Since typical spacecraft shielding attenuates protons with energies below 10 MeV [24], the predominantly lower-energy trapped protons present

above 3.8 R_E are generally ineffective in producing radiation-induced damage. Figure 5 also indicates that solar-flare-induced protons dominate from five to beyond fourteen R_E.

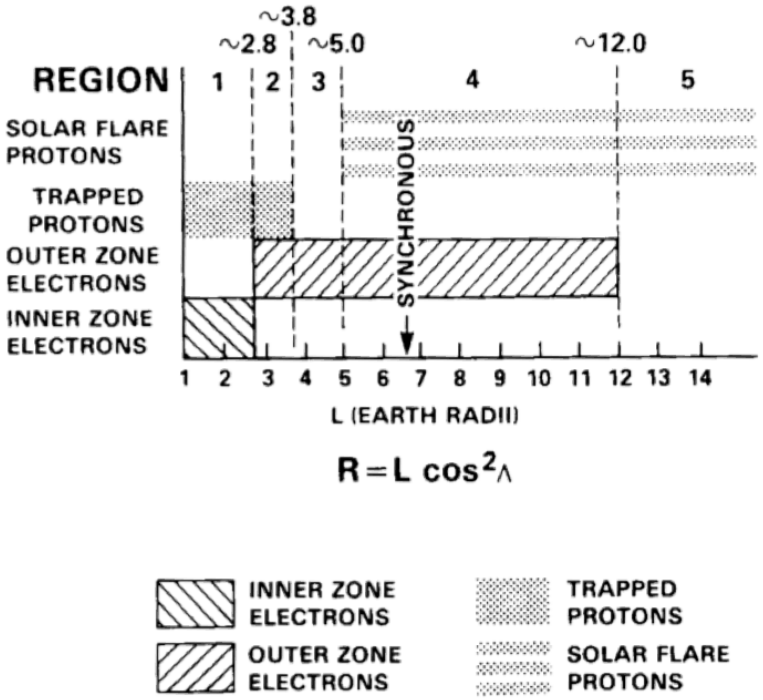

Fig. 5. Charged particle distribution in the earth's magnetosphere. The geosynchronous earth orbit corresponding to 6.6 earth radii is also indicated. After [23].

Trapped electrons predominantly exist from one to twelve R_E, with two distinct zones of existence depending on the corresponding electron fluxes. The inner zone electrons, extending from one to 2.8 R_E, have fluxes ten times lower than the outer zone electrons that extend from 2.8 to twelve R_E. The maximum energies of the trapped electrons are 5 MeV and 7 MeV respectively for the inner and outer zones, which makes the interactions between the electrons insignificant for single-event effects but an important consideration for total dose effects [19].

Cosmic rays originate either from the sun (solar cosmic rays or flares) or from outside our solar system (galactic cosmic rays or GCR). Solar flares, which are random events, mainly consist of protons (90-95%), alpha particles, and heavy ions. In a typical solar

flare, the proton and alpha particle composition dominate, while the heavy ion concentration is insignificant to that from GCRs. However, this can be dramatically altered in a large solar flare, where the proton and alpha concentrations can increase by 10,000 times of that in a typical solar flare, and the heavy ion concentration can rise up to 50% of the value of the background GCR [25]. The background GCR flux is minimum during solar flare maximum (periods of peak solar activity), and maximum at solar flare minimum (periods of least solar activity). Additionally, solar winds arising from solar flares have the potential to enhance the total dose received by a device in low-earth orbit by disturbing the geomagnetic fields and compressing them towards earth.

GCRs are omnipresent in space, dominating at all periods of time except when there are solar flares. GCRs consist mainly of protons (85%), alpha particles (14%), and high-energy heavy ions (less than 1%) [24, 26]. As the GCRs enter the magnetosphere, the low-energy portion of the spectrum at the low-earth orbit is attenuated. The flux spectrum of the GCRs is computed by using the Cosmic Ray Effects on Microelectronics (CREME96) [27] using the GCR algorithm specified in [28]. The GCR flux at the solar minimum describes the actual environment 40% of the time [19], as shown in Fig. 6. The Adams' 10% worst-case environment shown in Fig. 6 indicates an environment that is worse (than the Adams' environment) only for an additional 10% of the time [29], and includes contributions from both GCRs as well as solar flares. The Adams' environment is used to assess the single-event upset hardness of microelectronic devices.

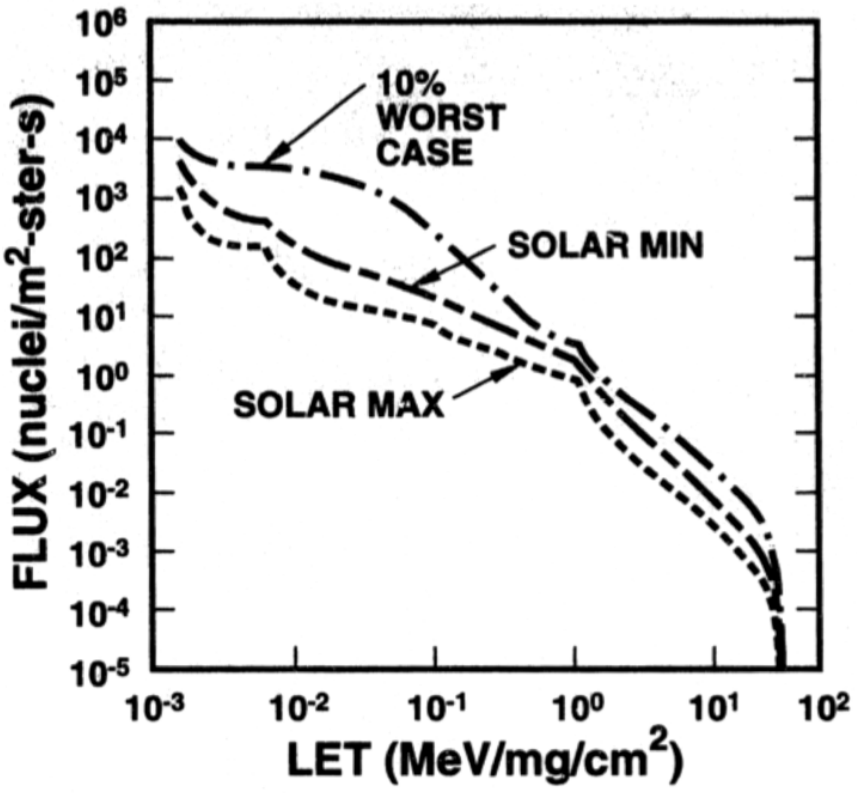

Fig. 6. Low-earth orbit magnetospheric GCR attenuation of electron flux as a function of electron energy and incident angle, for Si. After [23].

Radiation-effects research can be categorized into three main fields of study – total dose, displacement damage, and single-event effects. Total dose effects deal with the effects of accumulation of radiation dose on microelectronic devices. The dose accumulation induces undesirable changes in the device parameters. For a minority carrier device like a BJT, this could mean a lowering of gain due to excess hole injection into the emitter [30], while oxide and interface traps in a majority carrier device like a MOS transistor shift the threshold voltage and cause an nMOS device to become leakier postirradiation [31].

Displacement damage effects occur as a result of interaction of high-energy particles (for e.g., protons with energy > 3 MeV) with the semiconductor material. As the high-

energy proton collides with an atom while traversing through a semiconductor material, the atom is knocked free from its lattice site to an interstitial site. If the displaced atom has sufficient energy, it can in turn displace other atoms, leading to a defect cascade with large defect clusters. A typical cluster distribution produced by a 50 keV recoil atom is shown in Fig. 7 [32].

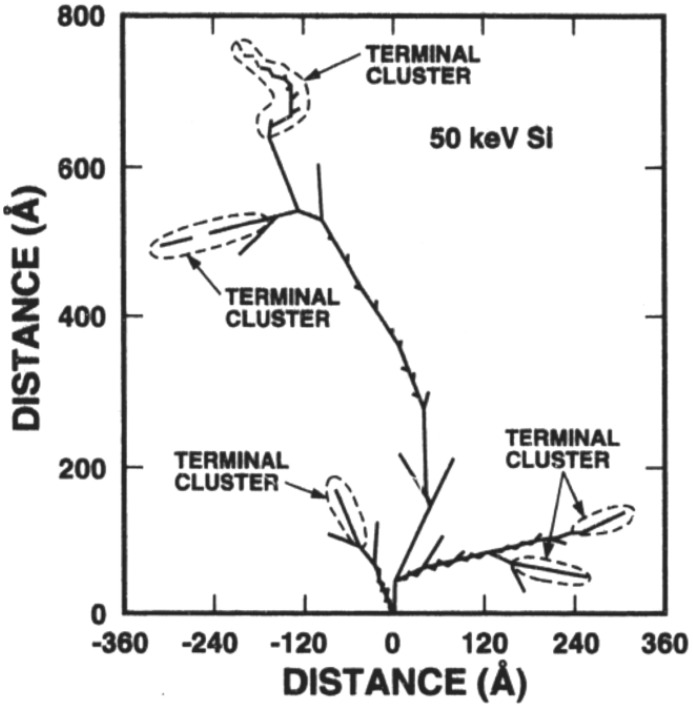

Fig. 7. Defect cascade resulting from a 50 keV silicon recoil atom. After [32].

The "terminal clusters" represent the large clusters of defects formed at the ends of the paths of the primary and reflected atoms, as they traverse through the silicon. The primary effect of displacement damage is the formation of deep and shallow-level traps in the material. While the shallow traps result in carrier removal by compensating for majority carriers, the deep traps can act as generation, recombination or electron/hole trapping centers, depending on their location [32-34]. This ultimately causes undesirable effects such as increase in the substrate resistance by decreasing carrier mobility,

reduction of minority carrier lifetime, thermal generation rate change of electron-hole pairs etc. Therefore, displacement damage is a concern primarily for minority carrier devices like bipolar transistors and optoelectronic devices [19].

Single-event effects relate to the changes caused in the output response of a microelectronic device due to interaction with an energetic particle traversing through the device. A single-event transient occurs when the charge generated from the energetic particle is collected at one of the device nodes/electrodes, resulting in a current pulse at the node, as shown in Fig. 8.

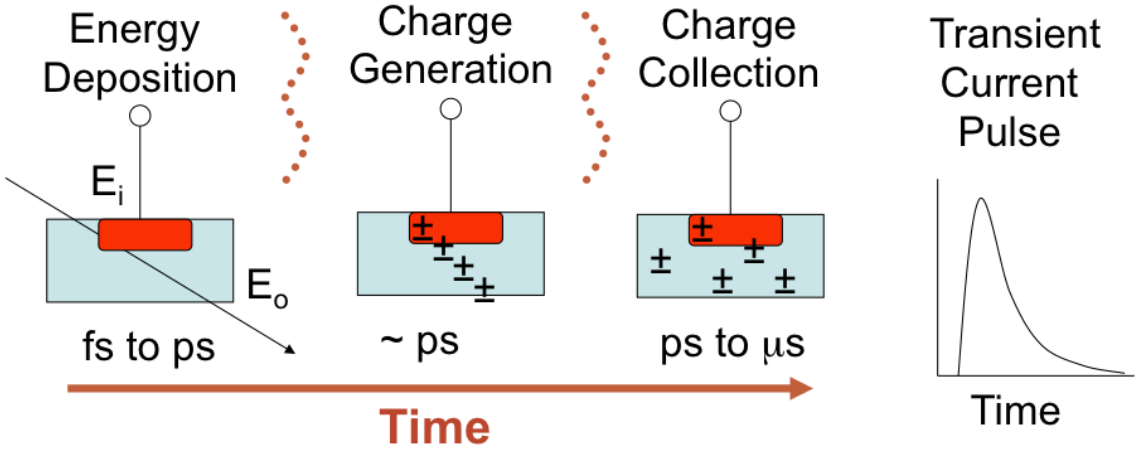

Fig. 8. The evolution of a single-event transient. After [35].

The number of single-event transients generated for a given fluence of the incident energetic particle defines the single-event cross section, which is a measure of the (single-event) sensitive volume of the microelectronic device. Mathematically, the single-event cross section can be expressed as follows:

$$\sigma = (\#\text{ single-event transients}) / \Phi$$

where σ and Φ correspond to the single-event cross section (expressed in units of cm^2) and the beam fluence in units of particles/cm^2, respectively.

The total collected charge is estimated by integrating a single-event transient pulse over its duration. The ratio of the deposited to the collected charge, called the charge collection efficiency, determines if charge is lost (e.g., recombination within the device) or an enhancement occurs due to amplification of the charge within the device. The latter is important in InAlSb/InAs/AlGaSb HEMTs as we shall see in the following sections.

D. History of radiation effects research on III-V HEMTs

(i) InAlAs/InGaAs/InAlAs HEMTs

Depletion mode InAlAs/InGaAs/InAlAs HEMTs on InP substrates have known to perform well both in terms of power dissipation and operating speeds [36-38], which make them attractive candidates for potential space applications. As seen from Figs. 9(a) and (b), the band structure of the InAlAs/InGaAs/InAlAs HEMT allows for both a 0.5 eV deep electron well in the channel (comprising a 2DEG at zero bias as indicated in the dotted profile of Fig. 9(b)) because of a type-I band alignment. Following a single-event strike, the accumulation of holes at the bottom of the InGaAs channel lowers the potential barrier between the source and gate, referred to as source-channel barrier lowering. This makes it easier for the electrons to be injected from the source into the channel and eventually collected at the drain. Experimental and simulation-based single-event transient characterization of InAlAs/InGaAs/InAlAs HEMTs [39, 40] shows that source-channel potential barrier lowering is primarily responsible for the total integrated charge obtained from drain current transients [12]. There exists a barrier for holes between the InAlAs barrier and the gate in these HEMTs due to the nature of the band lineup between

InGaAs and InAlAs as seen in Fig. 9(b). This results in the source-injection current being localized in the InGaAs well.

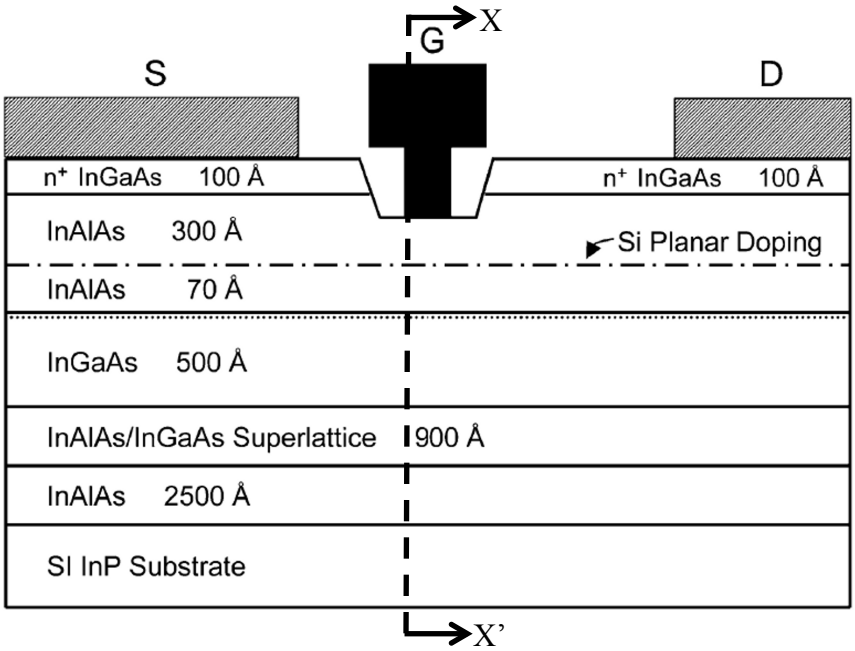

Fig. 9(a). Schematic cross section of an InAlAs/InGaAs/InAlAs HEMT. After [41].

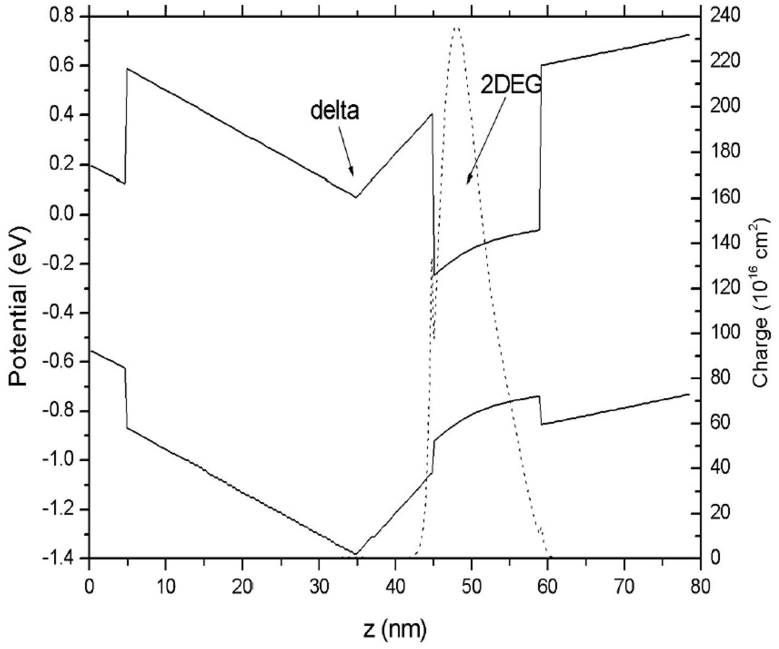

Fig. 9(b). Corresponding band diagram of the InAlAs/InGaAs/InAlAs HEMT obtained along cutline X-X' of Fig. 9(a). [41].

(ii) AlSb/InAs/AlSb HEMTs

This work has extended the initial single-event research on AlSb/InAs/AlSb HEMTs [11-13], which were the first antimonide III-V HEMTs to be commercially produced. While there have been a few published research papers on the radiation response of AlSb/InAs/AlSb HEMTs as described in the following sections, such is not the case with the relatively new InAlSb/InAs/AlGaSb HEMT. This HEMT is the central theme of the research and described in the following chapters.

Figure 10(a) shows the single-event (drain current) transient response from a laser strike on an AlSb/InAs/AlSb HEMT [11]; Fig. 10(b) shows the integrated charge as a function of the gate bias. The integrated charge varies non-monotonically with the gate voltage – as the magnitude of the gate voltage is reduced, the total integrated charge increases as the gate bias is increased from -0.7 V to near -0.55 V, and then decreases. The laser-induced[1] single-event response shown in Fig. 10(b) is attributed to injection of electrons from the source into the channel because of potential barrier lowering of the source-channel barrier, as shown in Fig. 11 [13]. The black equilibrium curve in Fig. 11 corresponds to the conduction band profile before the single-event strike occurs, while the red curve depicts the corresponding profile 20 ps after the peak of the strike in simulations.

After a single-event strike, the type-II band alignment in the AlSb/InAs/AlSb HEMT favors accumulation of holes underneath the channel in the AlSb buffer, and deposition of electrons in the channel. The influx of electrons in the channel and accumulation of holes in the buffer lower the potential barrier between the source and the channel. As a

[1] For top-sided laser irradiation, conversion factors of 1 to 3 pJ of laser pulse energy for 1 MeV-cm^2/mg heavy ion LET threshold have been suggested [42, 43]

result, electrons are injected over the lowered barrier from the source into the channel, as shown in Fig. 10(b).

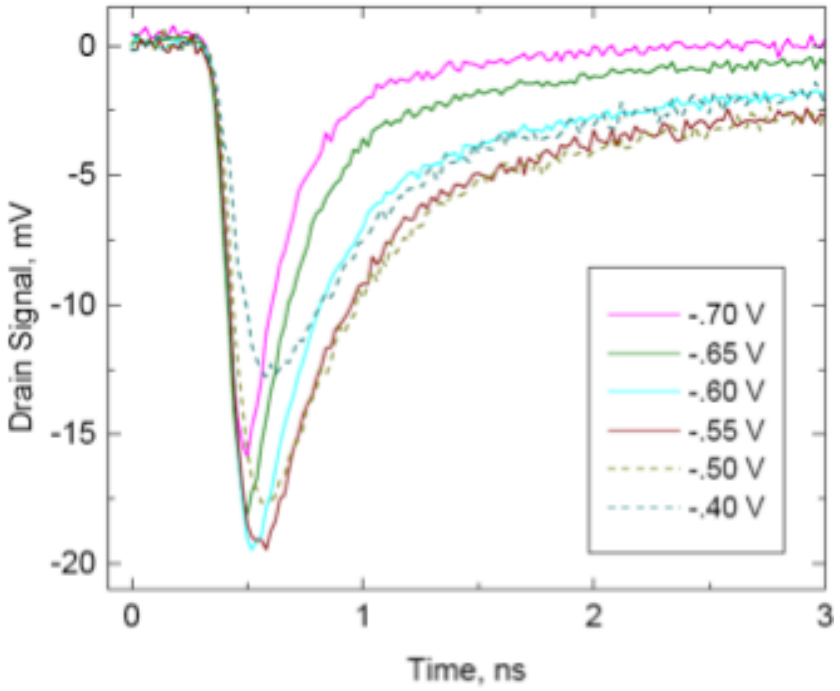

Fig. 10(a). Laser-induced drain current for different gate biases. L_{dc} = 2 µm, V_D = 0.25 V. After [11].

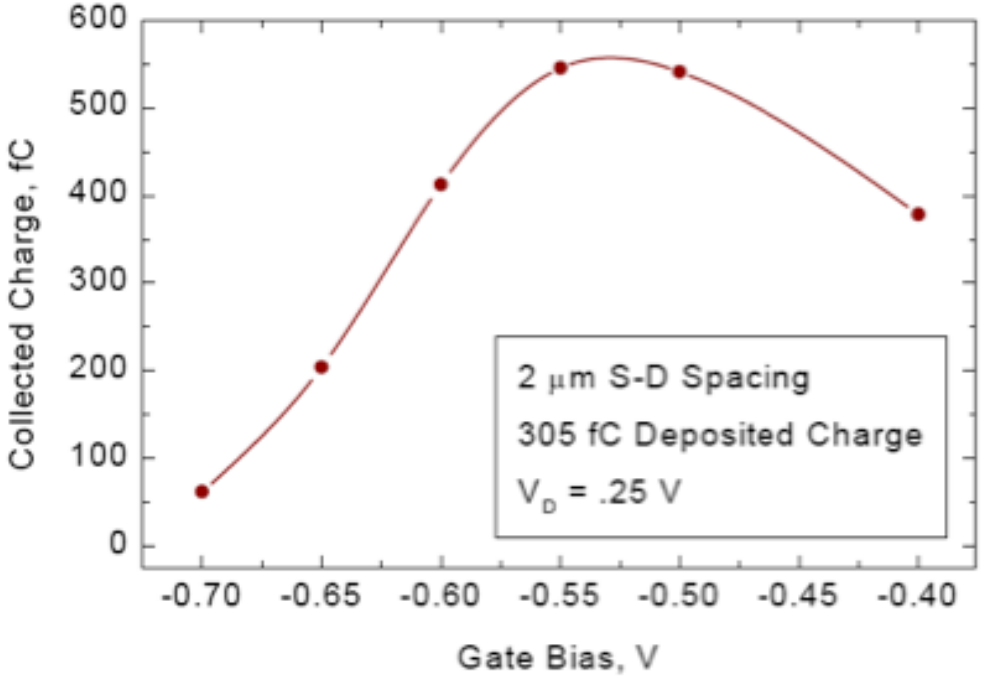

Fig. 10(b). Laser-induced integrated charge as a function of gate bias. After [11].

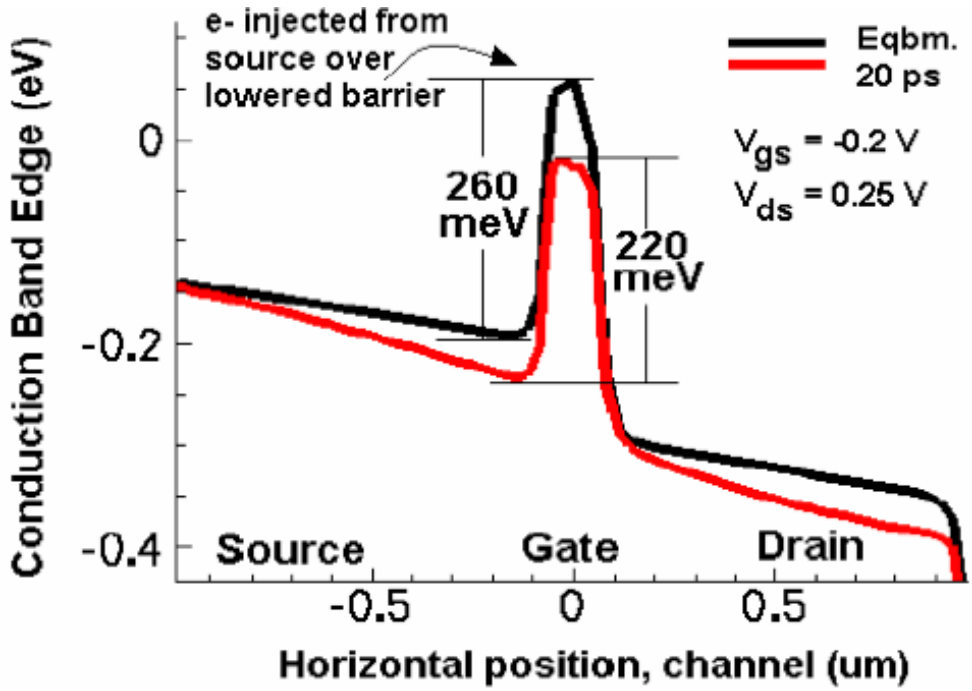

Fig. 11. Horizontal cutline through the channel showing source injection due to barrier lowering at source-gate edge in an InAs/AlSb HEMT. Initial barrier of 260 meV is reduced to 220 meV due to high influx of electrons in channel. Electrons are thus injected from the source the across lowered barrier. After [13].

Recently, the effects of process-induced variations on the single-event response of AlSb/InAs/AlSb HEMTs were reported [42]. These include variations in delta-doping, barrier and channel thicknesses and effect of carbon contamination in AlSb. As an example, Figs. 12(a) and (b) shows that higher delta-doping in the barrier contributes to more integrated charge at gate biases close to depletion than a corresponding lower delta-doping case since the former results in a negative shift of the threshold voltage, leading to incomplete pinchoff at a given (relatively high negative) gate bias. The source-to-drain charge injection due to source-gate barrier lowering [42] was chiefly responsible for the charge collection in all of these simulations.

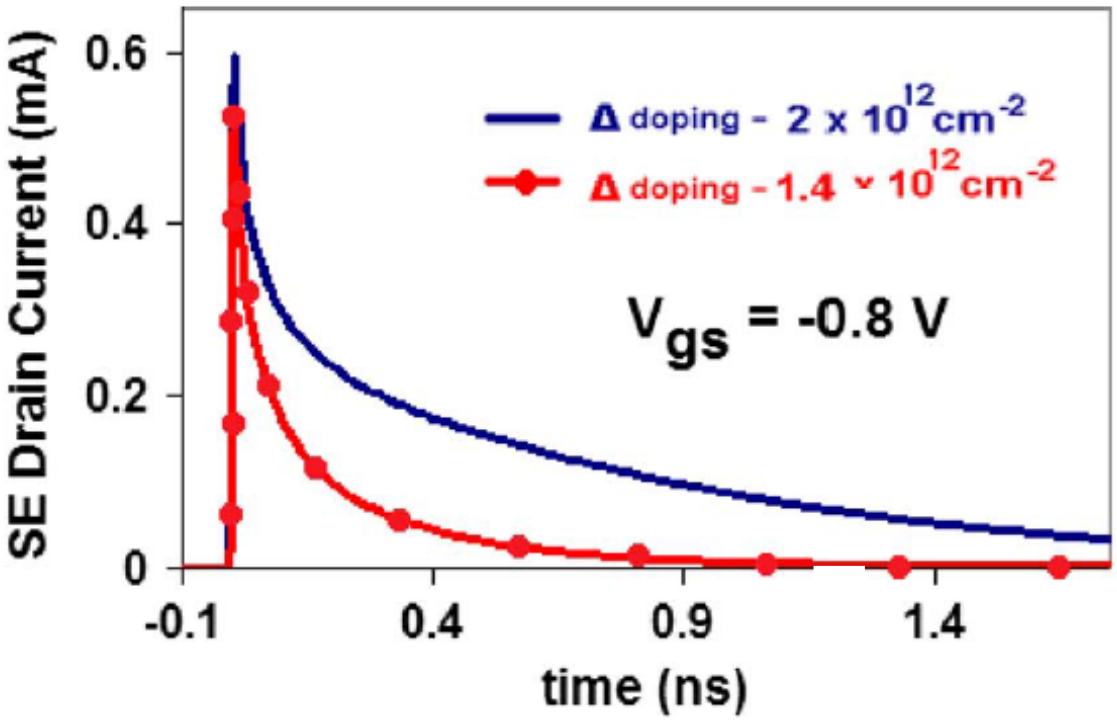

Fig. 12(a). Simulated single-event transients for two different delta-doping values, at depletion gate bias. Drain bias was 0.25 V. After [42].

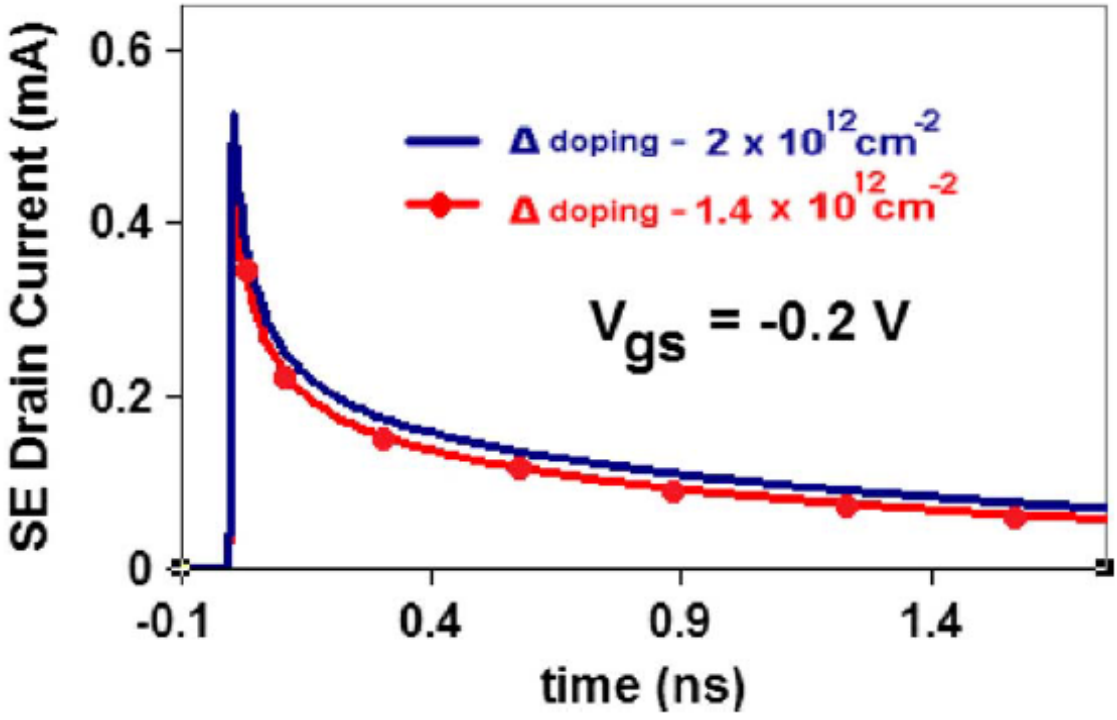

Fig. 12(b). Simulated single-event transients for two different delta-doping values, at strong accumulation gate bias. Drain bias was 0.25 V. After [42].

Similar to the delta-doping case, investigations into increased barrier and channel thicknesses lead to more negative threshold voltages, resulting in more integrated charge at high negative gate biases. Another finding pointed to the contribution of higher carbon contamination at the AlSb/SI GaAs heterointerface to lowered lower integrated charge because of increased surface recombination at the interface, resulting in reducing the corresponding transient tails [42].

AlSb/InAs/AlSb HEMTs have also been tested for total dose and displacement-damage effects [9], and have been found to be quite tolerant. 2 MeV proton irradiation of varying fluence was used in the tests with the HEMT biased in accumulation. Figure 13 shows a plot of the normalized drain current (ratio of unirradiated to irradiated drain current at corresponding fluence) as a function of drain voltage at zero gate bias. The drain current decreased with increasing proton fluence in a near-linear fashion. The switching behavior of the device under test (DUT) was found to be unaffected postirradiation. Weaver *et. al* [9] have postulated that the radiation-induced scattering affects and the carrier removal affect the corresponding mobility and 2DEG density in the channel, respectively, causing the observed decrease in the drain current.

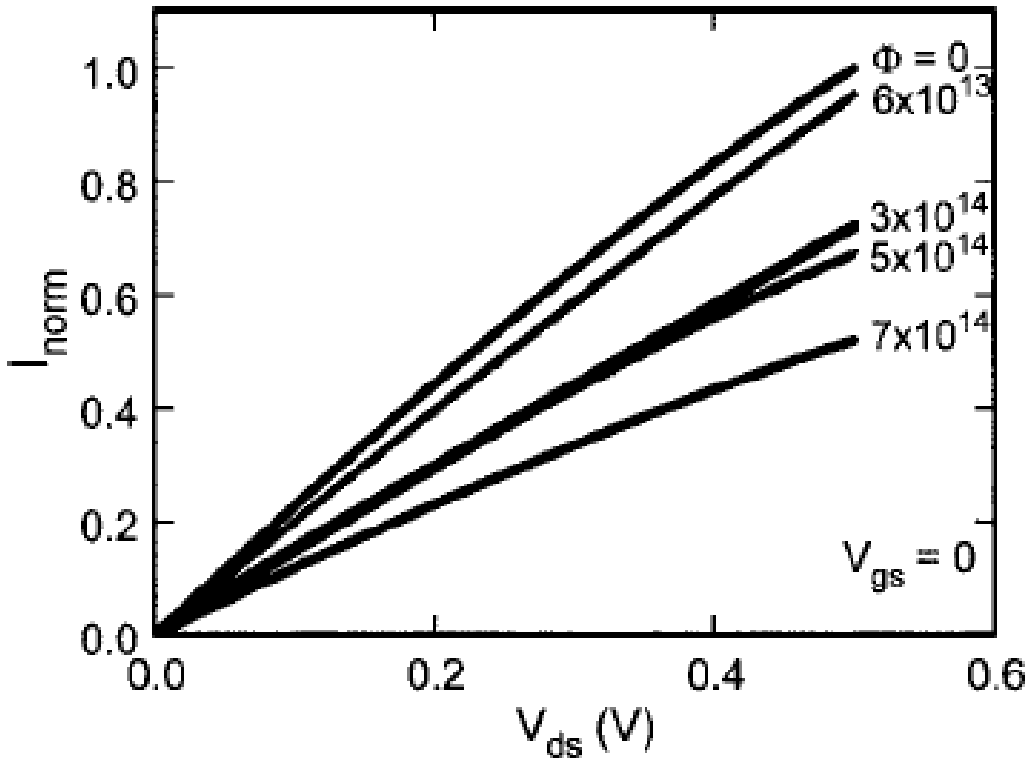

Fig. 13. Ratio of normalized (unirradiated to irradiated) drain current as a function of drain voltage for 2 MeV proton irradiation on AlSb/InAs/AlSb HEMTs. After [9].

The large ΔE_C between AlSb and InAs band edges that increase the probability of carrier reinjection, since it is energetically favorable for the carriers to fall back into the InAs channel from the AlSb buffer, after being removed from the channel. Thus, for a given fluence, the change in the corresponding drain current is relatively low in the AlSb/InAs/AlSb HEMT as compared to other HEMTs, as shown in Fig. 14 [9, 43].

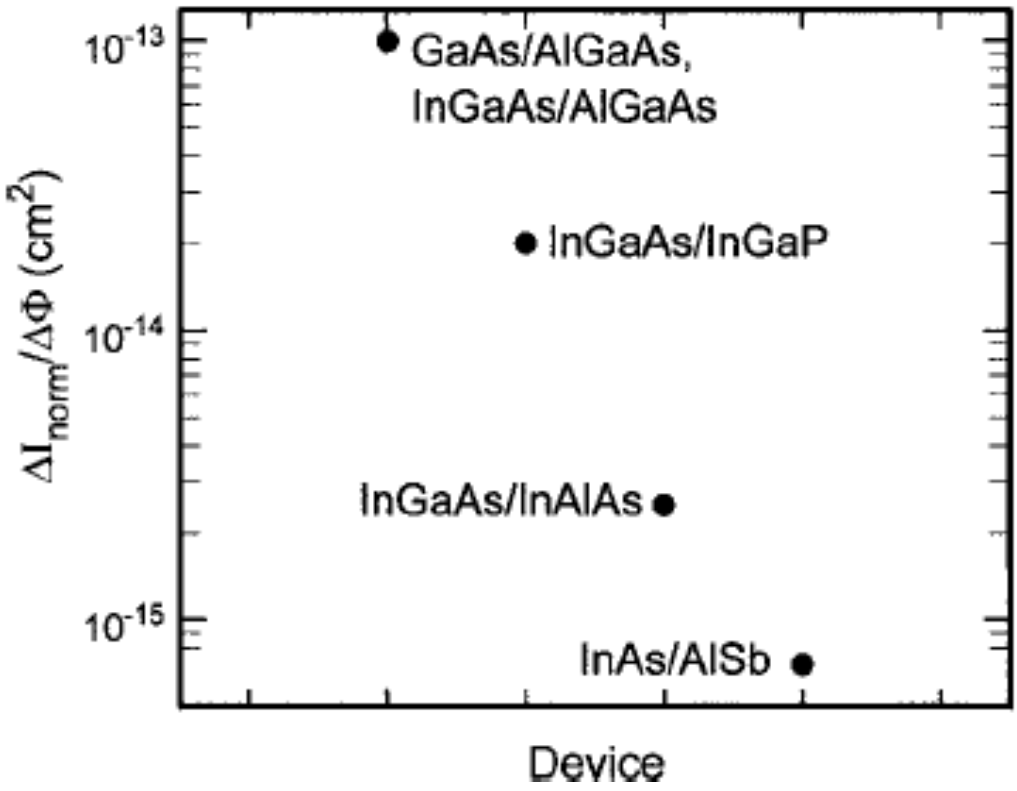

Fig. 14. Ratio of normalized (irradiated to unirradiated) drain current to total 2 MeV proton fluence at identical fluences, for various III-V technologies. After [9].

This chapter presented an overview of III-V antimonide HEMTs with InAs channels and introduced the InAlSb/InAs/AlGaSb HEMT. The basics of radiation effects in microelectronics were introduced and the history of single-event effects research on III-V HEMTs summarized. The next chapter focuses on the InAlSb/InAs/AlGaSb HEMT including processing and TCAD modeling details.

CHAPTER III

THE InAlSb/InAs/AlGaSb HEMT

A. Device processing

The development of InAlSb/InAs/AlGaSb HEMTs was first reported by Papanicolau and others [6] to improve the reliability and stability of AlSb/InAs/AlSb HEMTs. In this type of HEMT, the top InAlSb layer serves as a barrier to the InAs channel, which eliminates an extra processing step required for the growth of an $In_{0.5}Al_{0.5}As$ layer since AlSb is inherently well-protected from oxidation in the form of $In_{0.2}Al_{0.8}Sb$. Additionally, the strain between the $In_{0.5}Al_{0.5}As$ layer and the AlSb layer present in the AlSb/InAs/AlSb HEMT is absent.

A schematic cross-section of the device is shown in Fig. 15(a), while the actual cross-section of a processed HEMT is shown in Fig. 15(b). The corresponding band diagram obtained from a vertical cut through the center of a 2-D TCAD model of the InAlSb/InAs/AlGaSb HEMT is as shown in Fig. 3 of the previous chapter. Details of the modeled device are given in the next section. The device is grown on a semi-insulating (SI) GaAs substrate using a solid source molecular beam epitaxy on a Riber 21T system. First, the oxide is removed from the SI GaAs (100) substrate by exposing it to an As_2 flux at 630°C. The substrate temperature is then lowered to 500°C, followed by the serial deposition of the 1.5 μm $Al_{0.7}Ga_{0.3}Sb$ buffer, the 12 nm InAs channel, and the $In_{0.2}Al_{0.8}Sb$ spacer layers at that temperature.

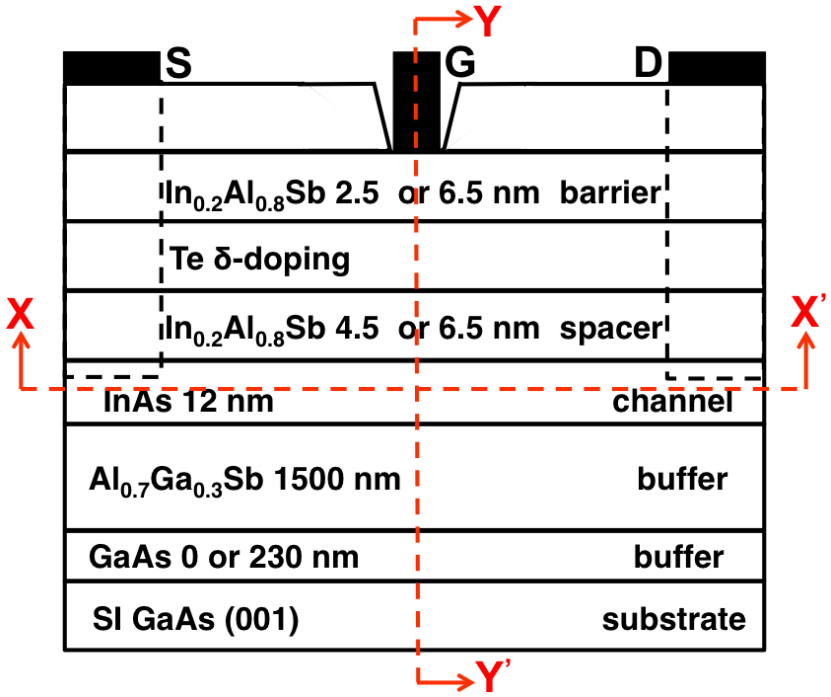

Fig. 15(a). Schematic vertical cross-section of an InAlSb/InAs/AlGaSb HEMT. After [7].

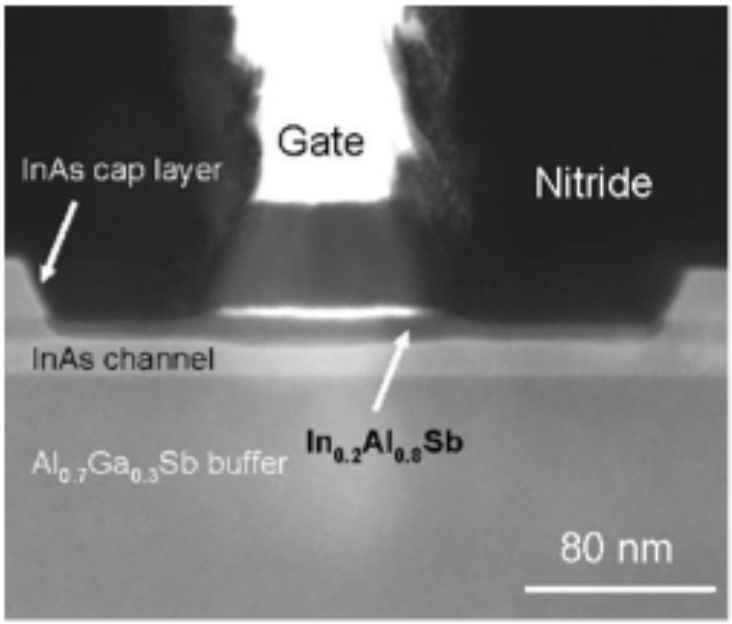

Fig. 15(b). Cross-section micrograph of an InAlSb/InAs/AlGaSb HEMT, obtained from cutline Y-Y' of Fig. 14(a). After [18].

The AlGaSb buffer accommodates the 7% lattice mismatch between the Si GaAs and the InAs channel. When the InAs channel layer is deposited, the SI GaAs thermocouple

temperature is ramped down by 40°C to compensate for the excess sample heating caused on account of the narrow bandgap InAs absorbing more heater radiation. The temperature is measured by transmission thermometry, and is accurate to within ±10% [7, 44].

The temperature is then dropped to 450°C, at which the serial deposition of the modulation doping layer, the InAlSb barrier, and the InAs cap layers is carried out. By using InAlSb instead of AlSb, cracking of the epitaxial layer due to oxidation (as shown in Fig. 15) is avoided [45]. Using InAlSb also obviated an extra processing step of depositing an extra $In_{0.5}Al_{0.5}As$ layer on top of AlSb, to avoid oxidation.

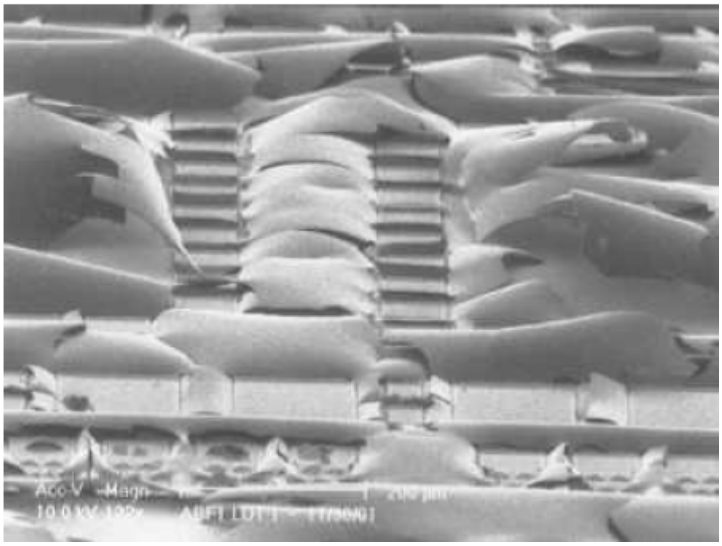

Fig. 16. SEM micrograph showing the oxidized and cracked AlSb barrier in an AlSb/InAs/AlSb HEMT. After [45].

The modulation doping of the InAlSb layer is carried out by either: (a) tellurium (Te) delta-doping using a GaTe cell (b) an arsenic soak or (c) silicon-doped InAs. For this HEMT, Te delta-doping is used at the reduced temperature of 450°C in order to reduce Te diffusion and segregation, with the GaTe cell being maintained at 600°C. The growth rate for the AlGaSb buffer and InAlSb barrier was 1 monolayer/s (ML/s), with that of the InAs channel being 0.4 ML/s. This corresponds to an unintentionally-doped channel with

a carrier density of $2 \times 10^{18}/cm^3$. The growth rates were calibrated by reflection high-energy electron diffraction (RHEED) oscillations. The arsenic for InAs was supplied from a Riber valved cracker, with the tip maintained at 950°C to produce As_2. Antimony for the buffer and barrier layers was produced by an Applied Epi valved cracker, with a 900°C tip temperature to produce Sb_2. In order to minimize As contamination in the buffer and barrier layers, the As valve is closed during the deposition of all Sb layers [7, 44].

The source and drain ohmic contacts are first defined by a polymethylmethacrylate (PMMA) resist and deep-UV lithography. Palladium/platinum/gold (Pd/Pt/Au) layers in the ratio 100 Å/200 Å /600 Å are then alloyed by e-beam evaporation and heat treated at 175°C for three hours on a hot plate located in a glove box containing a H_2:N_2 (5:95%) ambient [46]. Care is taken to ensure that the resulting contacts are smooth in surface morphology and surface definition, and have low contact resistance as measured by four-terminal clove-leaf van der Pauw measurements [47]. However, the actual diffusion depth of the alloy and the interface of the alloy and the AlGaSb buffer is not monitored, since the low contact resistance sets the tone in achieving good DC and RF response. Following the alloying of the source/drain contacts, an Au/TiW Schottky-gate metallization is formed using a tri-level PMMA e-beam lithography. Prior to deposition of the metal gate, a citric acid etch is performed on the exposed surface of the InAlSb barrier. In order to prevent gate leakage on account of the gate metal touching the mesa

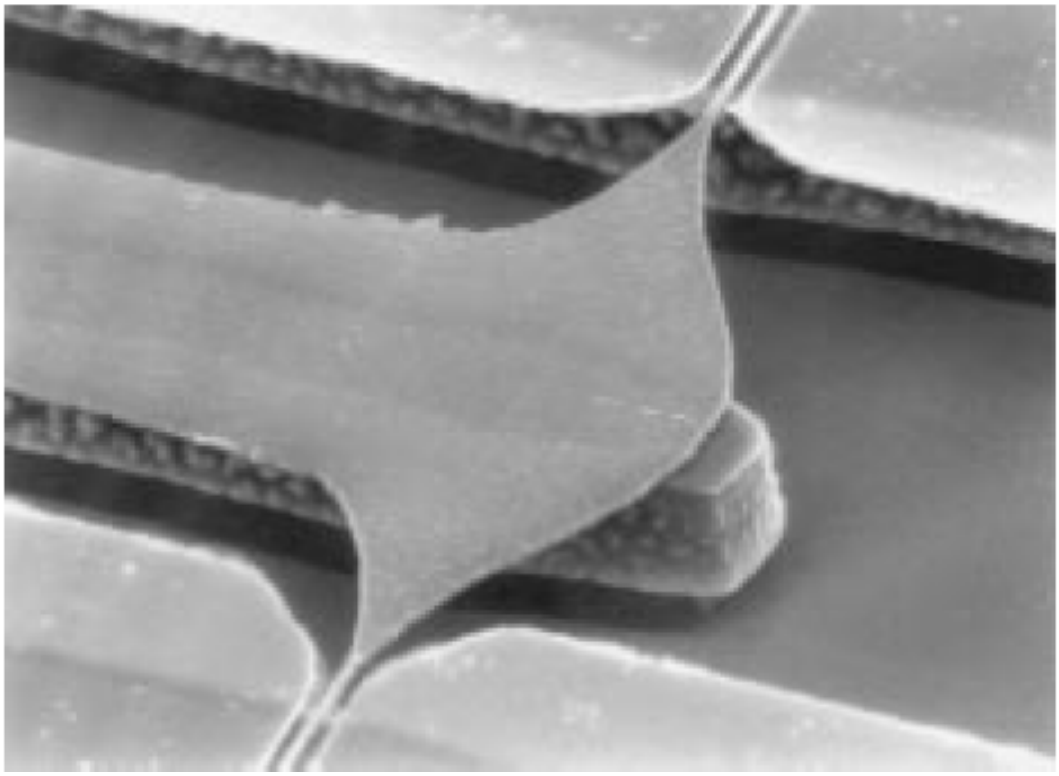

Fig. 17. SEM micrograph of an air-gate at the mesa edge of an InAlSb/InAs/AlGaSb HEMT. After [47].

sidewall, an air-bridge is formed between the channel and the gate bonding pad, as shown in Fig. 17. The air bridge is formed by undercutting the material beneath the mesa-exposed gate metal region by a hydrofluoric acid/peroxide-based etch [47].

B. Modeling

This section describes the 2-D TCAD model of the InAlSb/InAs/AlGaSb HEMT developed using the Synopsys [48] set of tools that was used to investigate device-level phenomena influencing the single-event response described in chapters IV, V, and VI in this dissertation in detail. Figures 18(a) and (b) show the cross-section of the model built. The electrical properties of all the HEMT materials were taken from the literature [49],

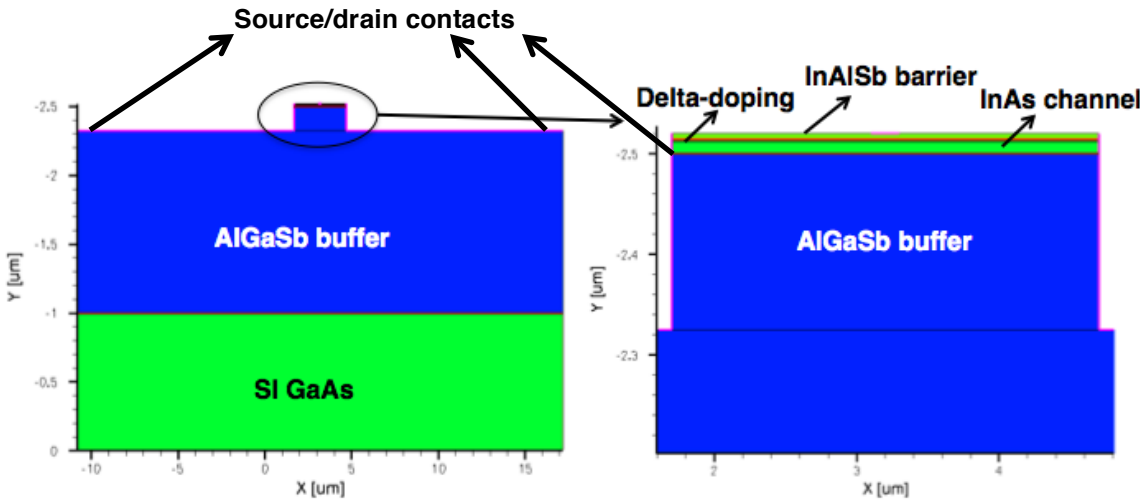

Fig. 18(a). 2-D TCAD model of the InAlSb/InAs/ AlGaSb HEMT.

Fig. 18(b) Close up of (a) showing the top layers.

and linear interpolation was used to calculate the corresponding electrical properties of the ternary antimonides, $Al_{0.7}Ga_{0.3}Sb$, and $In_{0.2}Al_{0.8}Sb$. A ΔE_C of about 1.1 eV between the InAlSb/AlGaSb and the InAs conduction bands forms, which is slightly lower than the 1.35 eV value in AlSb/InAs/AlSb HEMTs but still sufficient to ensure carrier accumulation in the well at zero bias. The InAlSb spacer on top of the channel (shown in Fig. 15(a)) exists to enable the Te modulation doping and lower ionized impurity scattering from Te. All simulations were done at the device level, and no process simulations were used. The relevant device properties obtained from measurements for a given processing condition (such as mobility, doping etc.) were incorporated into the device simulator, as described below.

The p-type doping in the InAlSb buffer was estimated to be $1 \times 10^{13}/cm^3$. This information was provided by NRL (where the HEMT was processed). This estimate is consistent with literature in which the Te activation energy in $In_{0.25}Al_{0.75}Sb$ was found to be very high – about 125 meV. Over the range from 10% to 40% aluminum concentration

in InAlSb, the donor levels in Te appear to form a very deep level below the conduction band. Based on the measured activation energy in this range, about 1% of the incorporated carriers contribute to conduction, and thus give rise to very high resistivity values [50].

The default concentration in AlGaSb has been shown to vary with both the temperature at which it is grown as well as the aluminum mole fraction. AlGaSb grown at 650°C on SI GaAs was shown to have default concentrations of $1.2 \times 10^{19}/cm^3$ and $5.7 \times 10^{18}/cm^3$ for $Al_{0.76}Ga_{0.24}Sb$ and $Al_{0.32}Ga_{0.68}Sb$, respectively [51]. Wang and others have reported unintentionally doped concentrations of $5 \times 10^{19}/cm^3$ and $2 \times 10^{18}/cm^3$, respectively, for $Al_{0.7}Ga_{0.3}Sb$ grown on SI GaAs at 680°C and 600°C respectively [52]. Chidley and others have reported a concentration of $9 \times 10^{17}/cm^3$ for $Al_{0.8}Ga_{0.2}Sb$ grown on GaSb [53]. No reported data exist for the specific aluminum concentration and growth temperature used in the HEMT in this research. However, all of the above studies reported the default conduction of the AlGaSb material grown to be strongly p-type. Based on the above and the fact that the unintentional doping in the buffer is not measured during the processing of the HEMT at NRL, a value of 5 x $10^{17}/cm^3$ with p-type conductivity was chosen as the starting value for the $Al_{0.7}Ga_{0.3}Sb$ used in the model.

The source/drain contacts were placed as shown in Fig. 18 to describe the alloying into the buffer on either side of the gate. The gate was designated to be a Schottky barrier, with a barrier of 0.68 V, as discerned from discussions with NRL. The source/drain contacts were designated Ohmic, with the portion in contact with AlGaSb buffer designated as a Schottky barrier.

This chapter described the device processing and corresponding 2-D TCAD modeling details of the InAlSb/InAs/AlGaSb HEMT. The next chapter details single-event experiments carried out on the InAlSb/InAs/AlGaSb HEMTs. The 2-D TCAD model developed from the device properties based on the processing conditions is used for corresponding analysis of the mechanisms responsible for the observed output response in the subsequent chapters.

CHAPTER IV

MECHANISMS OF SINGLE-EVENT TRANSIENTS IN InAlSb/InAs/AlGaSb HEMTS

As described in the previous chapters, InAlSb/InAs/AlGaSb HEMTs are attractive candidates for potential applications in space microelectronics because of their low power dissipation and very high operating speeds. However, the relatively recent development of the InAlSb/InAs/AlGaSb HEMTs meant that there were no data available characterizing its single-event response. Therefore, broadbeam and microbeam experiments were designed to understand the mechanisms of single-event response of InAlSb/InAs/AlGaSb HEMTs. In particular, the experiments were geared towards providing insights in three key areas: (a) identify regions vulnerable to single-events (b) the single-event charge collection trends in the channel and regions far removed from the channel, and (c) the sensitivity of the gate bias to single-event transients in InAlSb/InAs/AlGaSb HEMTs. Sections (a) and (b) are detailed in this chapter while section (c) is described in the Chapter V.

A. Broadbeam experiments

(i) Experimental setup

Broadbeam heavy ion experiments were performed at the Grand Accélérateur National d'Ions Lourds (GANIL), France, using both low-LET as well as high-LET Xe ions of 28 MeV-cm^2/mg and 65 MeV-cm^2/mg respectively. Data were collected on four HEMTs, which were mounted on customized high-speed transient capture packages [54], and transients resulting from the heavy ion strike were recorded using a Tektronix

DPO71604B sampling oscilloscope, coupled to the HEMTs through a Picosecond Labs' bias tee [55]. The data described below pertain to one of the four HEMTs used in the experiments.

(ii) Experimental results

Figure 19 shows single-event transients recorded in the experiments from a 2 × 150 μm × 0.2 μm InAlSb/InAs/AlGaSb HEMT. As seen in Fig. 19, the recorded single-event transients ranged from a few hundred picoseconds to over a nanosecond at full width half maximum (FWHM). The cross-section corresponding to the slower transients were similar to that of the channel region as shown in Fig. 20, which was consistent to that seen previously on AlSb/InAs/AlSb HEMTs [13]. The cross-section corresponding to the faster transients was considerably larger than the channel region (by up to five times), and were consistent with the source and drain contact area as shown in Fig. 20 [14].

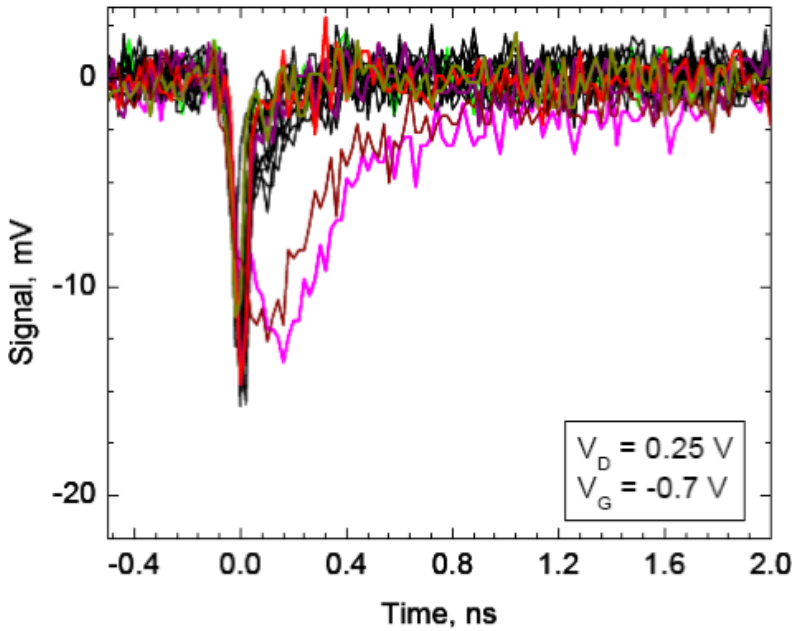

Fig. 19. Examples of fast single-event transients obtained from 28 MeV-cm^2/mg, 45 MeV/nucleon ^{132}Xe. After [56].

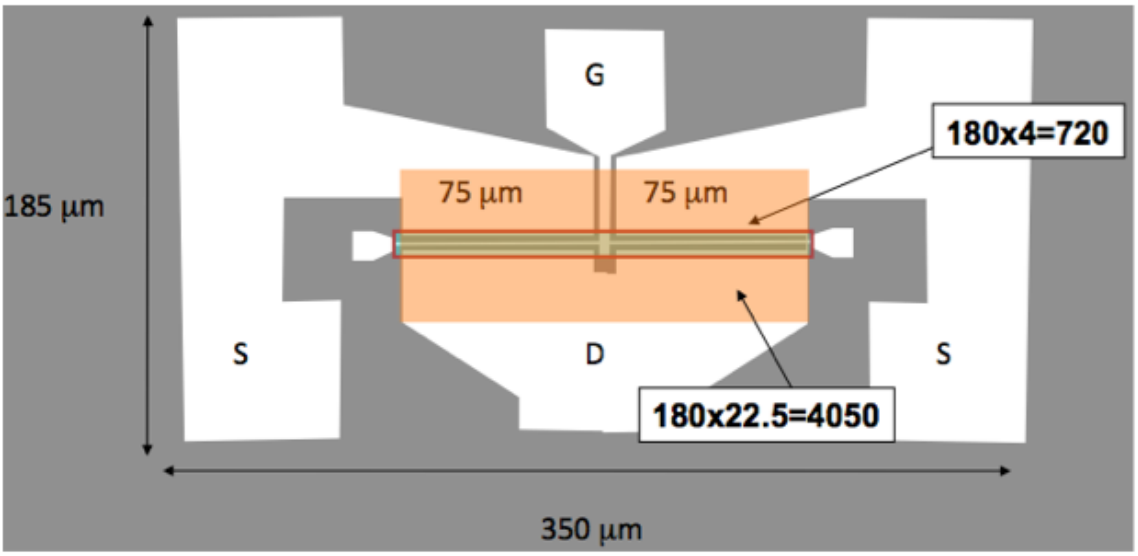

Fig. 20. Single-event cross-sections related to the source and drain contact areas for the broadbeam test on an InAlSb/InAs/AlGaSb HEMT. After [14].

Figure 21 shows the distribution of the single-event transient FWHM pulse widths for the transients with the relatively smaller and larger single-event cross sections. The "slow" and "fast" notations represent the respective longer and shorter single-event transients, with the more frequently-occurring faster transients primarily associated with those generated away from the channel, on the source and drain pads. These experiments thus showed that it was possible to produce single-event transients not only from the channel region but also from regions far removed from the channel. They also indicated that the interface between the source/drain contact alloy and AlGaSb buffer had a role in generating single-event transients as a result of an ion event traversing through it. The following sections describe the modeling and experiments carried out to confirm that the alloy-buffer interface could indeed produce single-event transients.

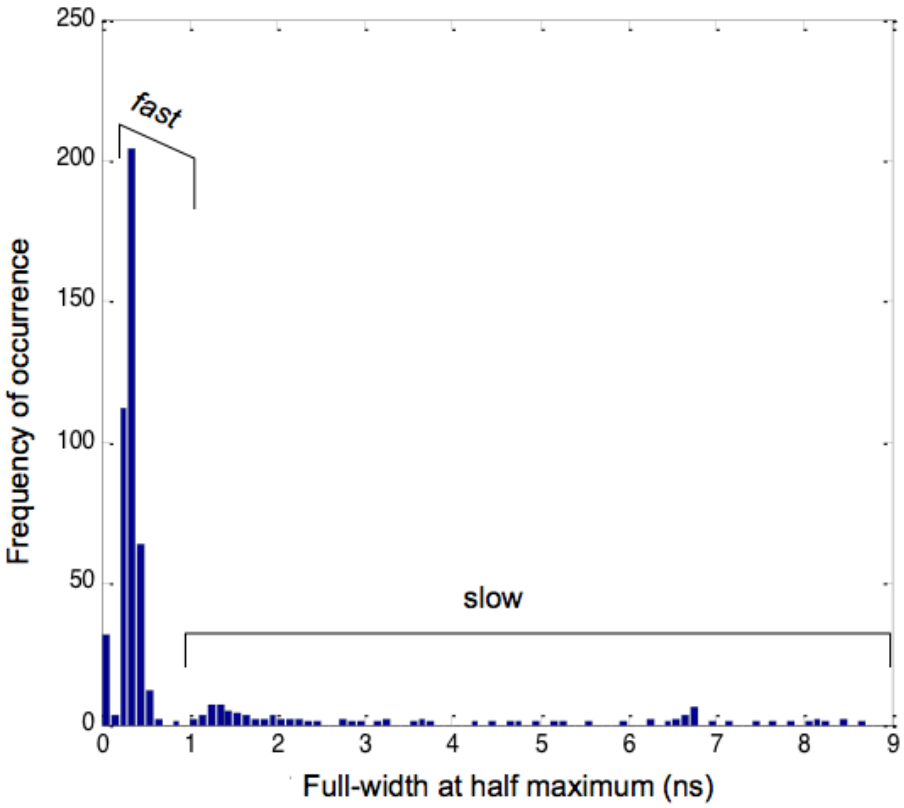

Fig. 21. Distribution of single-event transient pulse widths for events in both the channel as well as regions removed from the channel in InAlSb/InAs/AlGaSb HEMT. After [56].

(iii) Modeling SETs produced by ion events across the alloy-buffer interface

As detailed in the previous chapter, the source/drain alloy diffusion interfaces are not actively monitored during device processing. Instead, contact resistance is measured, with low values (e.g., 0.08 Ohm-mm [2]) taken as an indication of achieving good 2DEG control through the alloy. A study conducted on the reliability of the Pd/Pt/Au alloy in InAlSb/InAs/AlGaSb HEMTs showed decreased contact resistance with increasing Pd diffusion into the AlGaSb buffer [57], represented as Pd-Al-Ga-Sb in Fig. 22. Further, Fig. 22 reveals that the alloy/buffer interface is ragged and Pd diffuses and intermixes with part of the buffer region like a semiconductor impurity. While this may not affect

standard device operation (i.e., low contact resistance values would be maintained), these characteristics

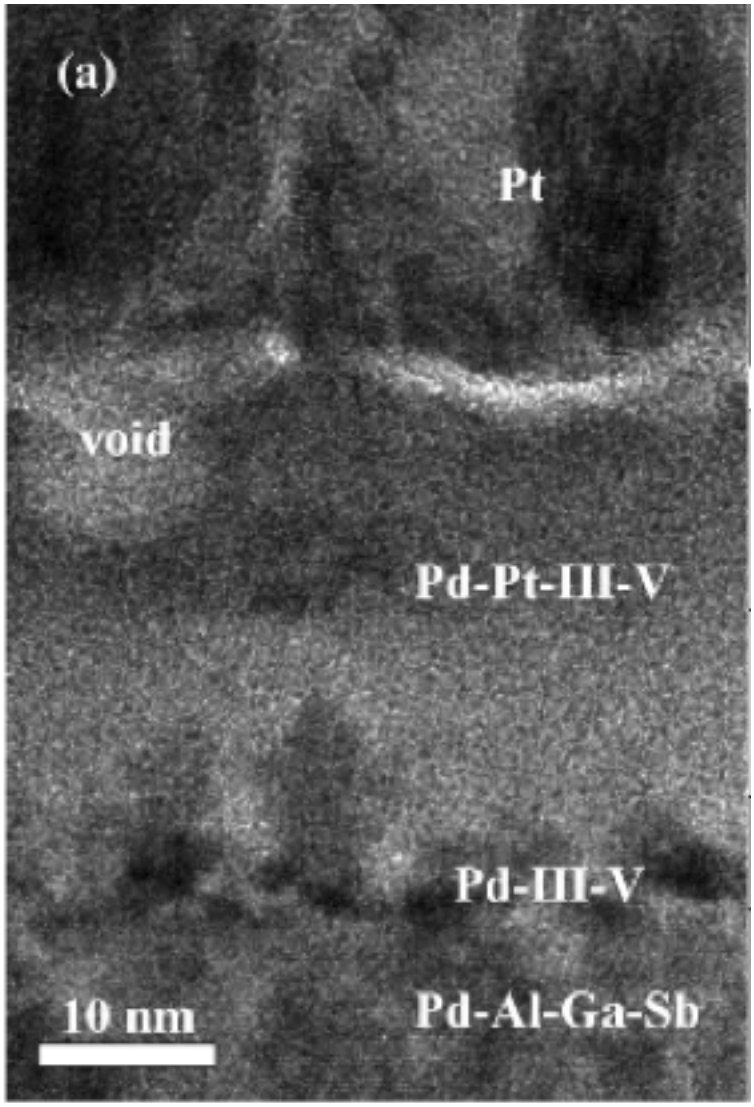

Fig. 22. TEM cross-section of an InAlSb/InAs/AlGaSb HEMT showing Pd diffusion into the heterostructure as well as the AlGaSb buffer. After [57].

strongly affect the corresponding single-event response. If the contact between the drain region and the buffer layer behaves as a Schottky barrier, there will be an electric field at the interface. Therefore, an energetic ion passing through this interface will produce a transient as the electron-hole pairs recombine after being separated by the electric field.

2-D TCAD simulations were performed to determine if a Schottky-barrier at the alloyed contact-buffer interface could generate fast transients similar to those measured experimentally. The simulated structure, including the equivalent circuit of the model 5542 40 GHz bias tee from Picosecond labs [55] connected to the drain and gate contacts of the 2-D TCAD device structure is depicted in Fig. 23. The properties of the contact were defined by adjusting the workfunction where the alloy contacts the unintentionally doped p-type AlSb buffer. A doping density of $5 \times 10^{17}/cm^3$ was used, consistent with

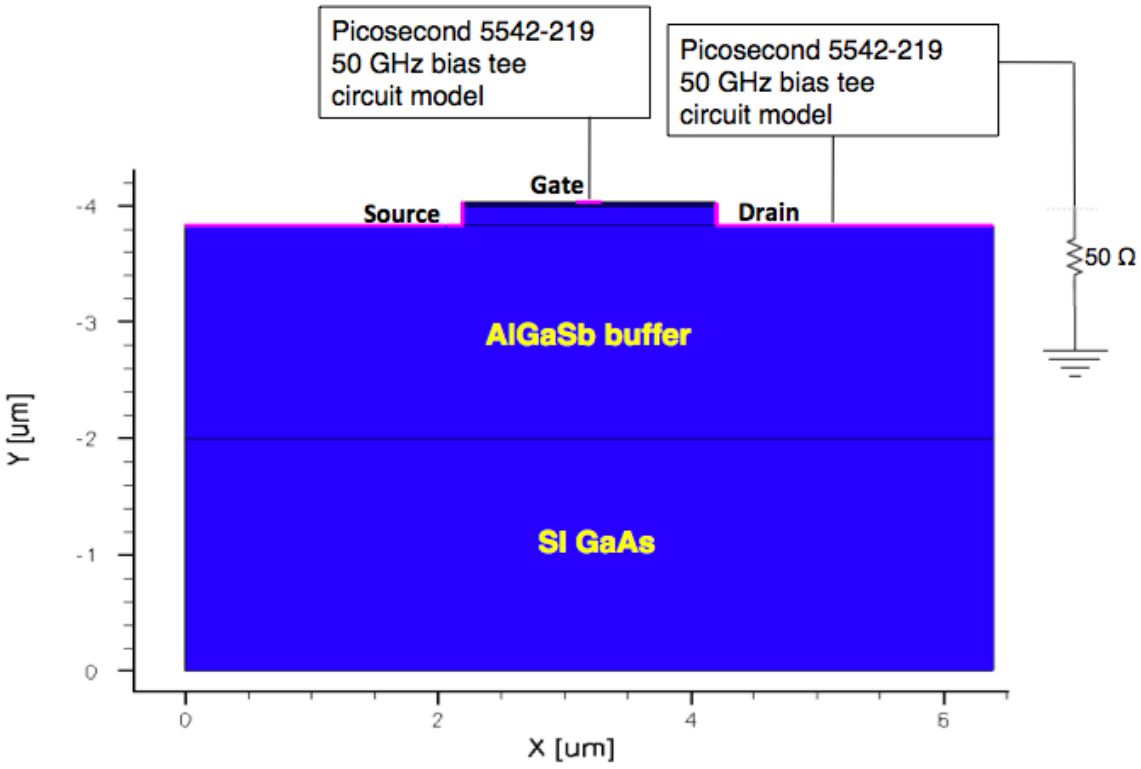

Fig. 23. 2-D TCAD simulation model that includes the bias tees and the load resistance emulating the 50 Ω termination on the oscilloscope.

reported values for unintentionally doped p-type AlSb [58, 59]. The simulated ion strikes were incident on the drain-side of the contact with Gaussian functions defining the strike spatially and temporally. Figure 24 shows the drain transient profile obtained from a

strike into the drain contact. The transients observed for strikes to the drain contact have a full-width half maximum (FWHM) pulse width of 75 ps, similar to those seen in the experiments.

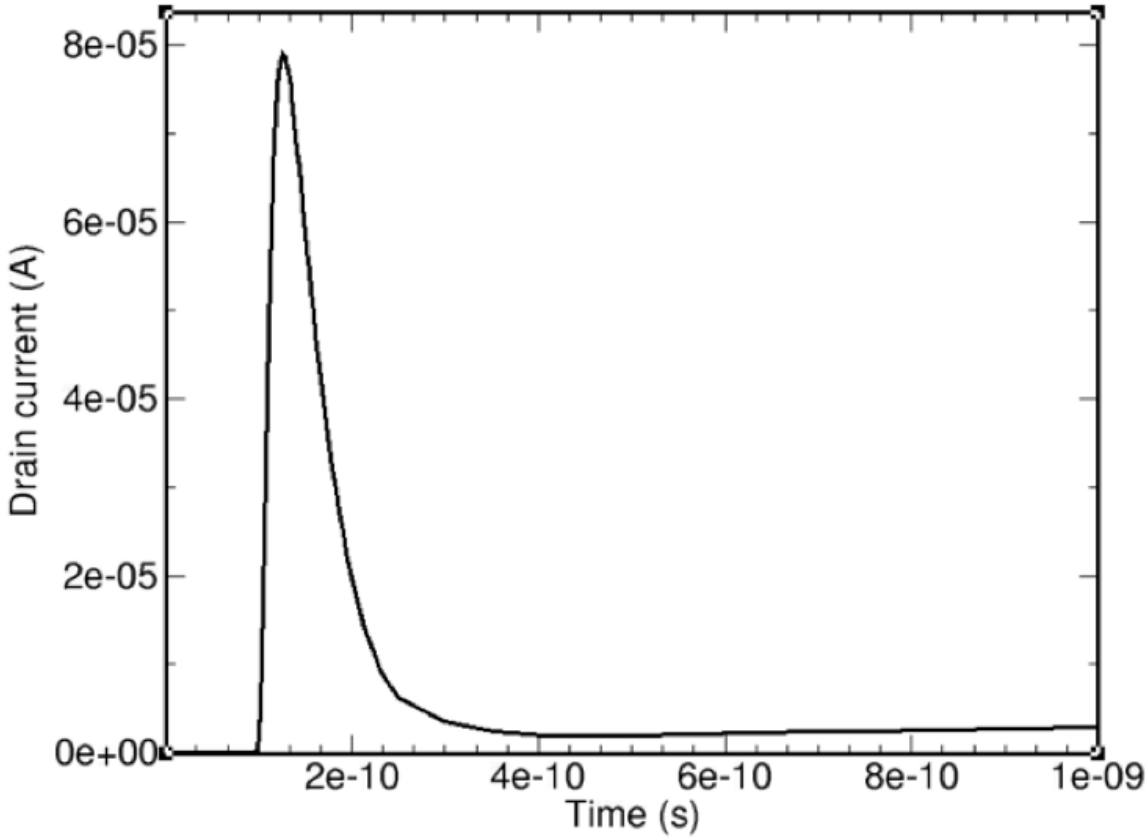

Fig. 24. Simulated transient profile obtained from a strike on the drain contact of a 2-D TCAD AlSb/InAs/AlSb HEMT. After [14].

The simulation results thus showed that single-event transients could be generated in regions away from the channel, when an energetic ion traverses through the drain alloy-buffer interface. The simulations also confirmed that the generation of single-event transients was possible in a device with realistic device properties in buffer doping, contact workfunction etc., and had the potential to increase the single-event cross section as seen in the experiments [14].

B. Microbeam experiments

The microbeam heavy ion setup at Sandia National Labs was used, with transient ion-beam-induced charge collection (TRIBIC) microscopy being the method of measuring and recording single-event transients [60-62]. The setup consisted of a magnetic lens that focused the beam exiting a van de Graaff accelerator, and an electrostatic beam scanning capability that allows the resulting 1.5 μm^2 beam spot to be scanned across the surface of the device under test (DUT). Additionally, a Tektronix DPO72004 real-time digital phosphor oscilloscope with 16 GHz of hardware analog bandwidth and 50 GS/s on all four input channels was used for transient capture.

The ion x-y raster on the device under test was carried out in 200 nm steps, with a map of the ion-induced transient information being recorded with position. The scan window size was nominally 30 μm × 30 μm, and was extended when required. The scan windows were chosen such that they included the active area (between the source and drain) as well as the pads on top of the respective alloyed source/drain contacts. A 42.3 MeV (0.67 MeV/nucleon) copper ion with an LET of 27.5 MeV-cm^2/mg was used in collecting data from the DUTs. The effective gate (V_G-V_T) and drain (V_D) biases were maintained at -0.25 V and 0.25 V respectively, with V_G, V_T, and V_D representing the gate bias, threshold voltage, and drain bias of the HEMT, respectively. The experimental DC characteristics of the InAlSb/InAs/AlGaSb HEMT are shown in Fig. 25. The DC characteristics were monitored continuously throughout the experiments and did not vary from their preirradiation characteristics.

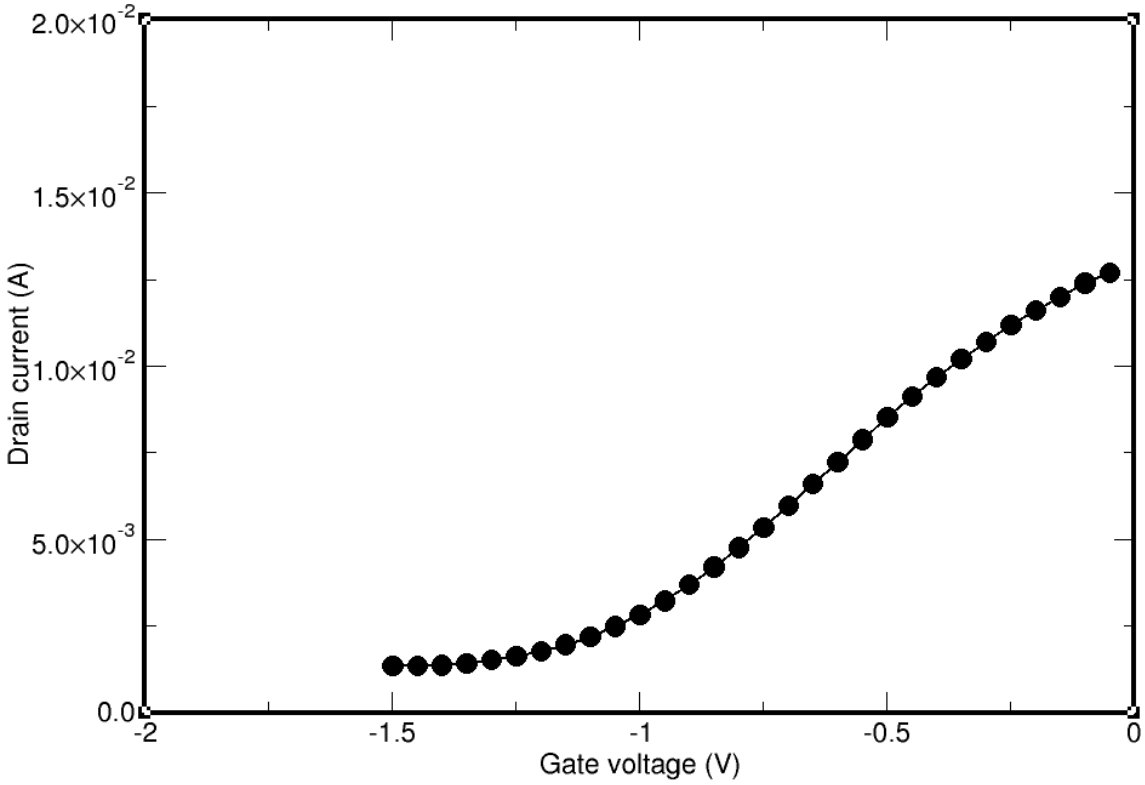

Fig. 25. DC characteristics of the InAlSb/InAs/AlGaSb HEMT used in the microbeam experiment. The drain bias was 0.25 V.

C. Microbeam test results

Figure 26 shows the spatial distribution of transient FWHM pulse widths obtained from the microbeam tests. Experimental evidence was obtained showing the presence of single-event transients on the drain pad of an InAlSb/InAs/AlGaSb HEMT. Additionally, it was also observed that the active area produced a majority of the observed single-event transients in the HEMT. Snapshots of the drain current transients in the drain pad and active region are shown in Figs. 27 and 28.

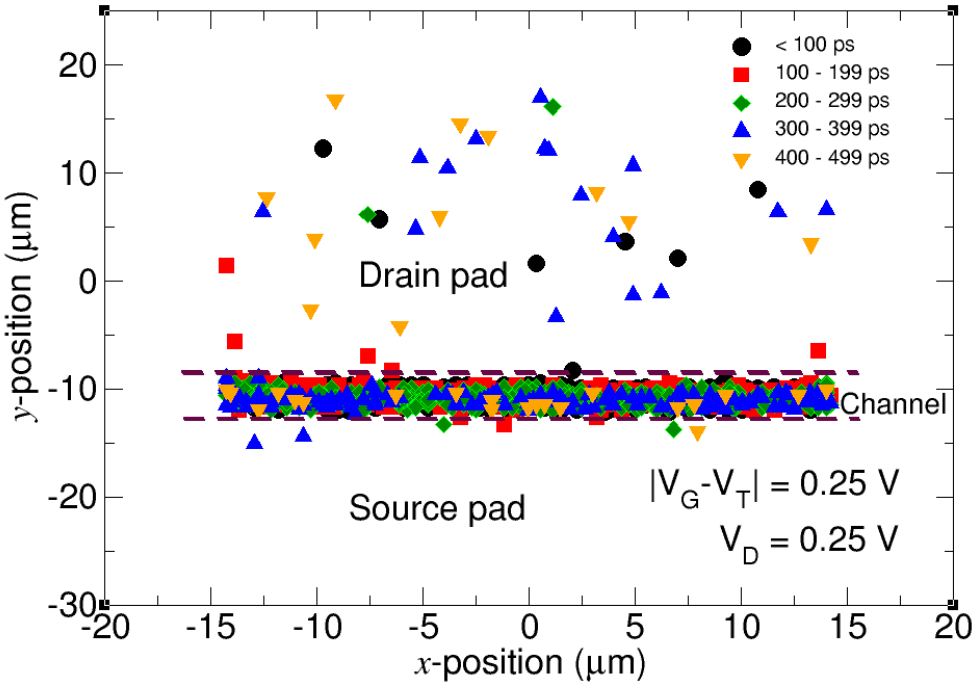

Fig. 26. Microbeam-induced transients seen on both the channel as well as the drain pad on an InAlSb/InAs/AlGaSb HEMT.

The location of the transients in Figs. 27 and 28 were picked randomly, and were for identical effective gate voltage and drain biases of -0.25 V and 0.25 V respectively. The transients on the drain pad were seen to have larger amplitude as compared to that in the active (channel) region. However, there were no specific trends in either the FWHM pulse widths or the integrated charge values. The FWHM pulse widths ranged from tens to hundreds of picoseconds in both the channel and drain pad regions, as seen in Figs. 26 through 28. The experiments thus not only proved that the drain pad could produce transients but also that the active region could produce transients of varied FWHM pulse widths and integrated charges.

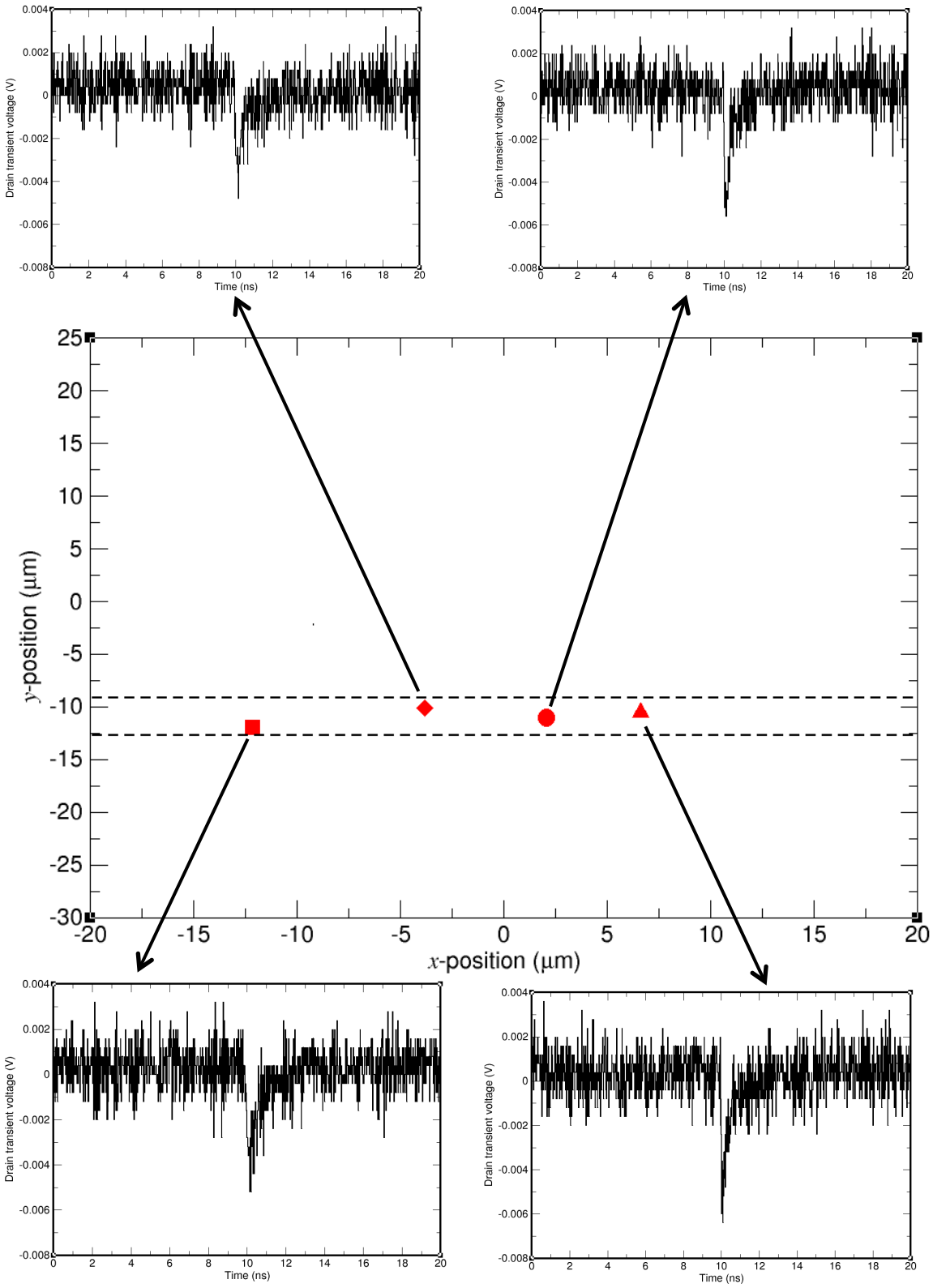

Fig. 27. Snapshots of transients recorded in the channel (active area) of an InAlSb/InAs/AlGaSb HEMT. The effective gate and drain biases were -0.25 V and 0.25 V respectively.

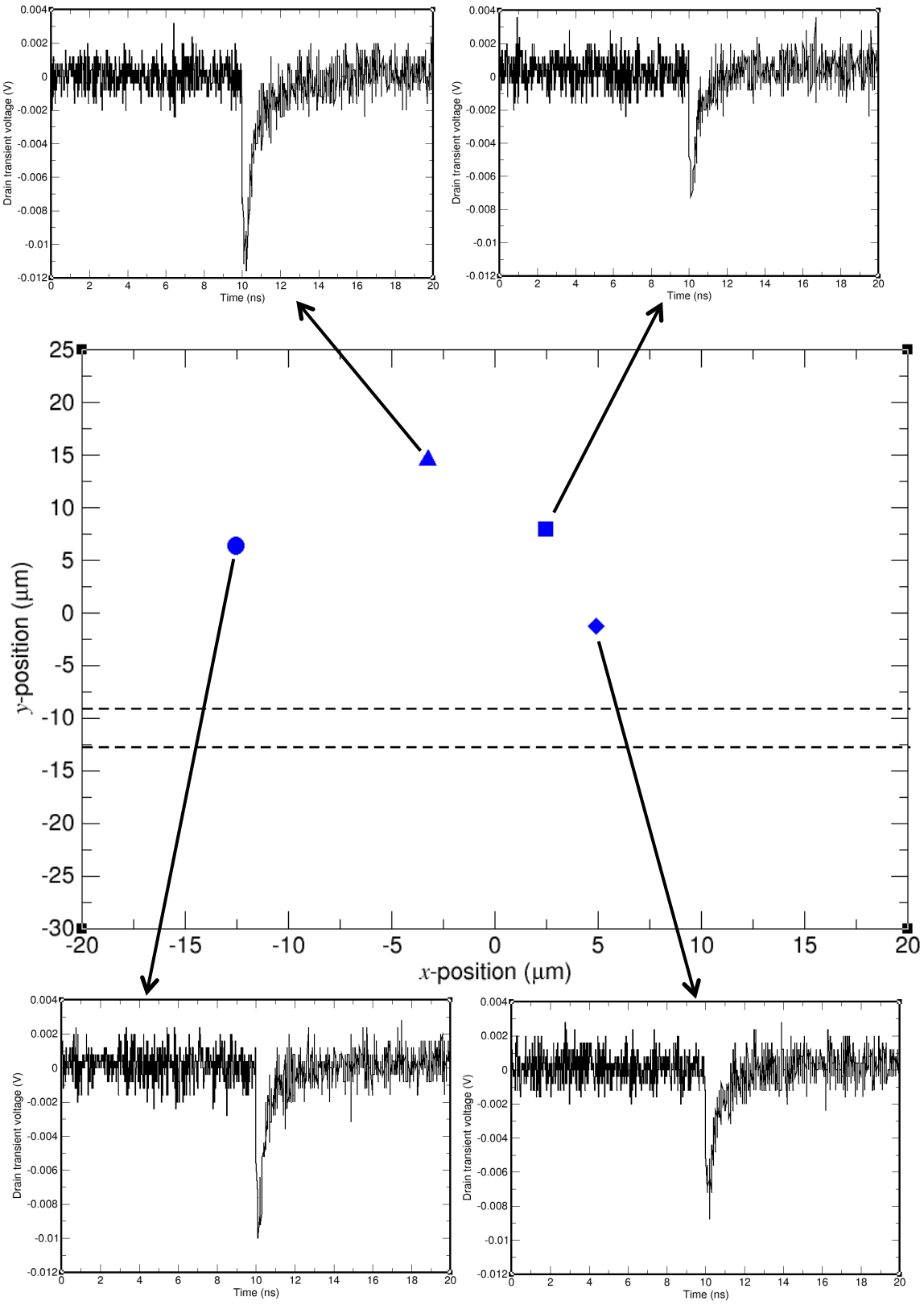

Fig. 28. Snapshots of transients recorded in the drain pad of an InAlSb/InAs/AlGaSb HEMT. The effective gate and drain biases were -0.25 V and 0.25 V respectively.

This chapter provided the first set of experimental single-event data on InAlSb/InAs/AlGaSb HEMTs. The data revealed it was possible to produce single-event cross-sections comparable to the size of the drain and source pads. Corresponding 2-D TCAD simulations based on the above broadbeam data postulated that a non-ideal drain alloy-buffer interface could produce transients on the drain pad. Microbeam experiments validated the above postulate and also showed that the active region of an InAlSb/InAs/AlGaSb HEMT produces most of the single-event transients with varied FWHM pulse-widths and integrated charges. The next chapter examines the single-event transient sensitivity to gate bias through experiments and simulation.

CHAPTER V

SINGLE-EVENT TRANSIENT SENSITIVITY TO GATE BIAS IN InAlSb/InAs/AlGaSb HEMTs

The previous chapter demonstrated how ion strikes to the drain alloy/buffer interface produce single-event transients and increase the single-event cross-section of InAlSb/InAs/AlGaSb HEMTs to encompass more area than that of the active region (between the source and drain) alone. The effect of gate bias on the corresponding integrated charge and cross-section in these HEMTs will be discussed in this chapter. The gate bias directly controls the electron density in the channel, which in turn modulates the drain current and hence, the corresponding single-event response. This chapter examines the single-event transient sensitivity of integrated charge and cross-section to gate bias. Single-event integrated charge and cross-section trends on four InAlSb/InAs/AlGaSb HEMTs with varied V_T values are determined as a function of effective gate bias. Experiments and 2-D TCAD simulations are used to explain the observed results.

A. Broadbeam experiments

Broadbeam experiments were carried out at Lawrence Berkeley National Labs. Four InAlSb/InAs/AlGaSb HEMTs with three different V_T values (-0.55 V, -0.6 V, and -0.7 V) were tested at room temperature. For all the experiments, 1 GeV Kr having an

LET of 25 MeV-cm^2/mg(Si) was used at normal incidence. All experiments were conducted in air. Kr was chosen since it was energetic enough to penetrate through the entirety of the device after passing through two millimeters of air, which was the distance between the DUT and the point of exit of the Kr ion beam in the vacuum chamber. The measured DC characteristics of the four HEMTs are shown in Fig. 29.

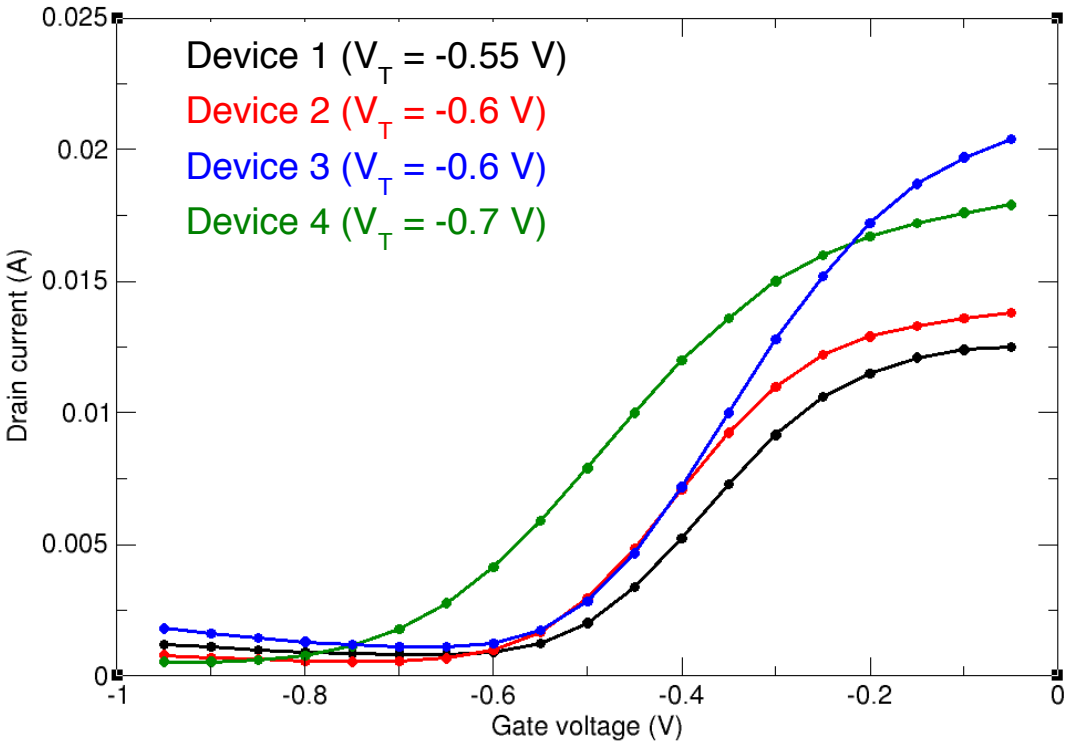

Fig. 29. DC characteristics of the four HEMTs used in the broadbeam experiments. The drain bias was 0.25 V for all devices. The V_T of each device is indicated.

Figure 30 shows the setup for the broadbeam experiments. Each HEMT was mounted on a customized high-speed transient capture package [54] shown in Fig. 31, and transients resulting from the heavy ion strike were recorded using a Tektronix TDS6124C oscilloscope. The HEMTs were tested for their DC characteristics at every stage of the experiments to ensure that their DC characteristics remain unchanged. Following these tests, the HEMTs were biased at a fixed DC gate and drain voltage and the ion beam was

turned ON. Each single-event transient produced was recorded and stored on the oscilloscope. The average flux and fluence values for each HEMT were 5×10^5 ions/cm^2/sec and 1×10^8 ions/cm^2, respectively.

Fig. 30. Broadbeam experimental setup at LBNL. The HEMT is mounted on a high-speed package and placed along the beam line (top of the picture).

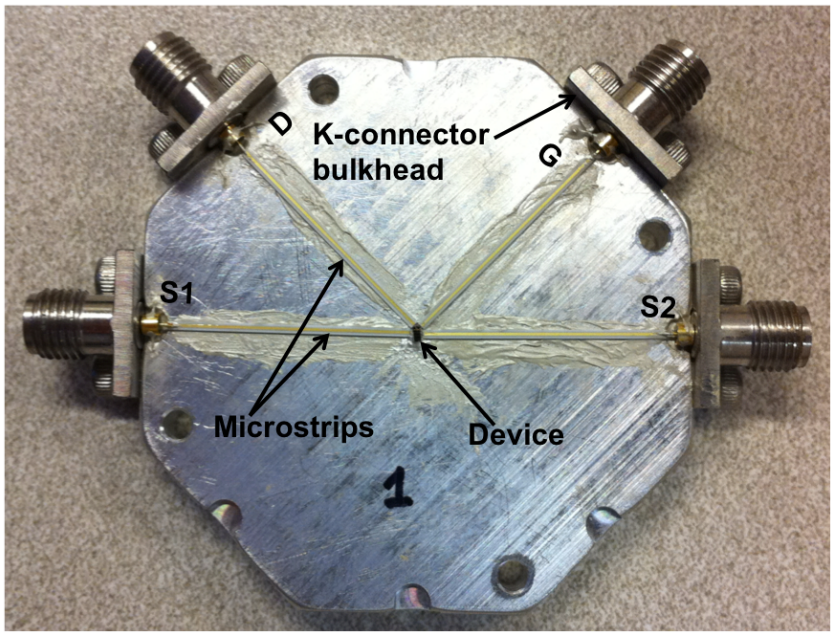

Fig. 31. A high-speed transient capture package similar to that used in the broadbeam experiments with the HEMTs.

B. Experimental results

Figures 32(a) and (b) plot the single-event integrated charge and cross-section values, respectively, as functions of effective gate bias. The data were measured using a constant drain bias of 0.25 V. The experiments show that the integrated charge and single-event cross-sections peak around V_T, and fall off on both the depletion as well as accumulation sides. At high accumulation effective gate biases of 0.3 V and above, there were no transients recorded on some HEMTs, resulting in zero integrated charge and limiting cross-sections, as shown in Figs. 32 (a) and (b).

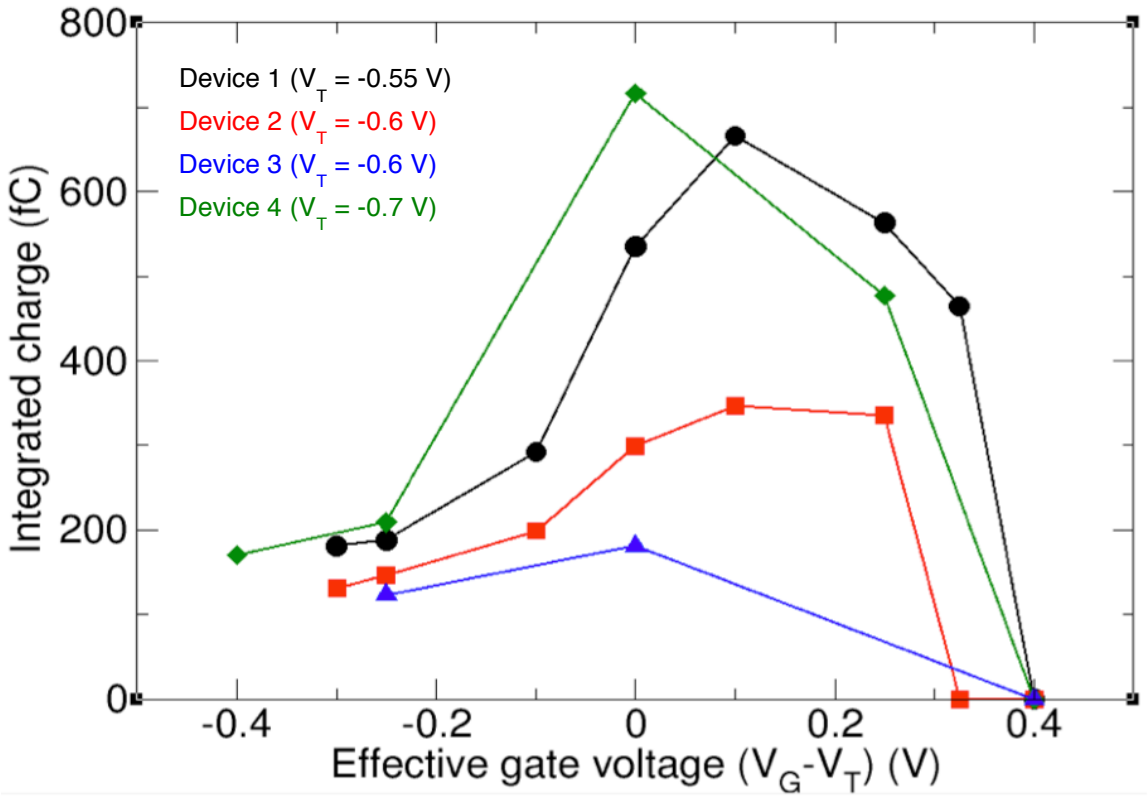

Fig. 32(a). Room temperature single-event integrated charge as a function of effective gate voltage measured using Kr broadbeam at LBNL. The V_T of each device is as indicated on the plot.

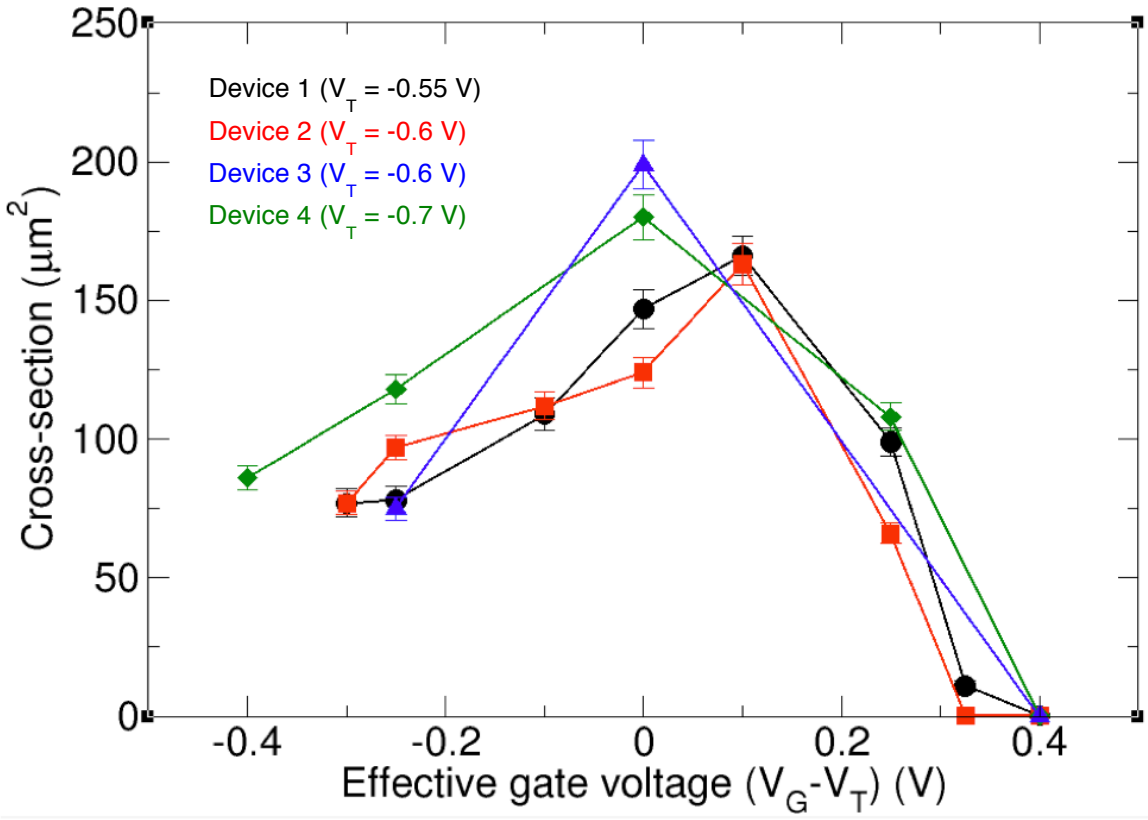

Fig. 32(b). Room temperature single-event cross-section as a function of effective gate voltage measured using Kr broadbeam at LBNL. The V_T of each device is as indicated on the plot.

Figure 33 shows a sample of three transients collected for Device 1, for three respective effective gate biases, viz. depletion, V_T, and accumulation. The transient profiles clearly show that the V_T bias condition accounts for both the highest amplitude as well as the longest pulse as compared to those at depletion and accumulation bias conditions. This translates into the V_T bias having the largest integrated charge amongst the three bias conditions, as evident from Fig. 32(a). Since these data were taken from a broadbeam experiment, Fig. 33 does not provide an insight into the location of the generated transients, but underscores the strong single-event sensitivity of the drain current transients to gate bias in InAlSb/InAs/AlGaSb HEMTs.

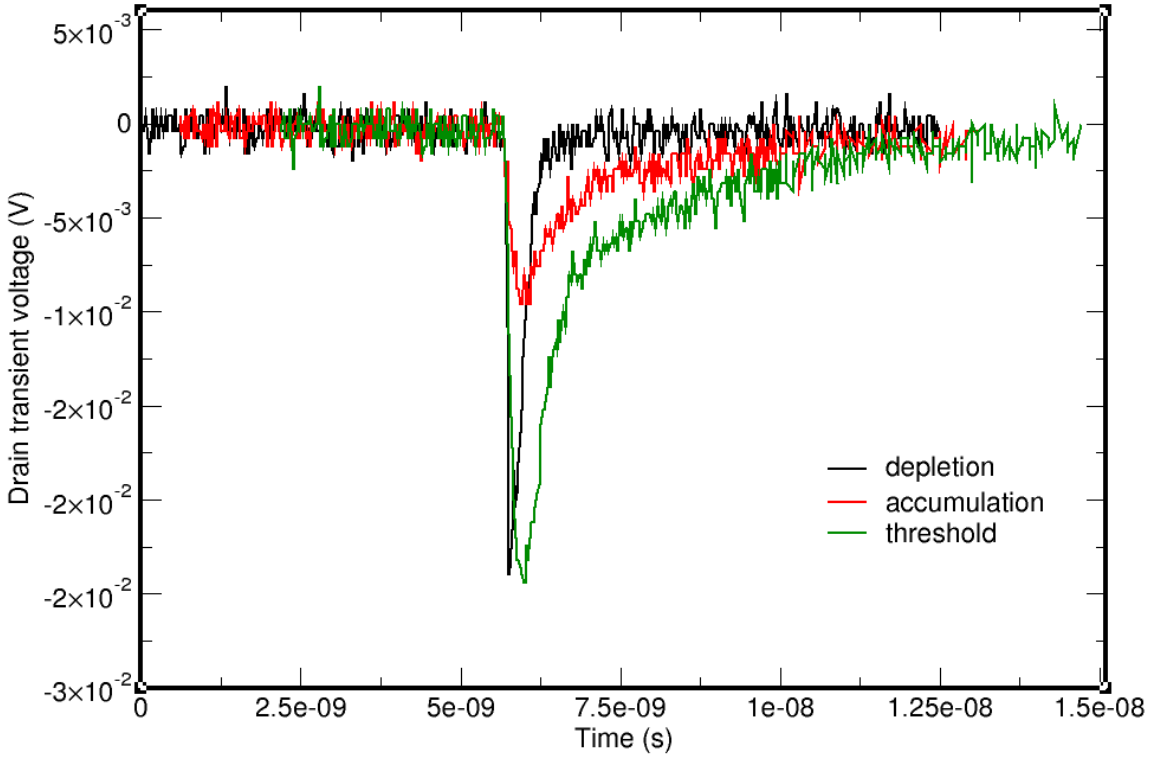

Fig. 33. A sample of three collected transients at three effective gate biases for Device 1.

C. Modeling methodology

2-D TCAD modeling and simulation analyses were performed to understand the mechanisms responsible for the observed integrated charge response. The simulation setup was identical to that used in modeling the alloy/buffer interface as described in Chapter III.

Single-event strikes with an LET value of 25 MeV-cm^2/mg (identical to that used in the experiments) were simulated, with strikes in the channel region between the gate and drain. The strike traversed through the entirety of the device, i.e., the barrier, channel, buffer, and SI GaAs substrate. The simulations used a constant deposition of the chosen LET along the track of the ion strike [48]. All simulations were carried out with the Picosecond 5542-219 bias tee circuit model [54] included as in the experiments, as shown

in Fig. 23 of Chapter IV. The 50 Ω resistance at the output of the drain bias tee represented the oscilloscope termination resistance in the experiments.

The simulations allow one to discern the single-event charge collection mechanisms in the InAlSb/InAs/AlGaSb HEMT. 2-D TCAD simulation models of the HEMT were used throughout the work, with drain currents per unit area matching within ±1% of that in an actual device, as shown in Fig. 34.

D. Model implementation

Figure 34 shows the DC characteristics of the simulated 2-D TCAD model of the InAlSb/InAs/AlGaSb HEMT, compared with that of Device 1 used in the experiments. The DC (drain) current increases as one goes from depletion towards accumulation.

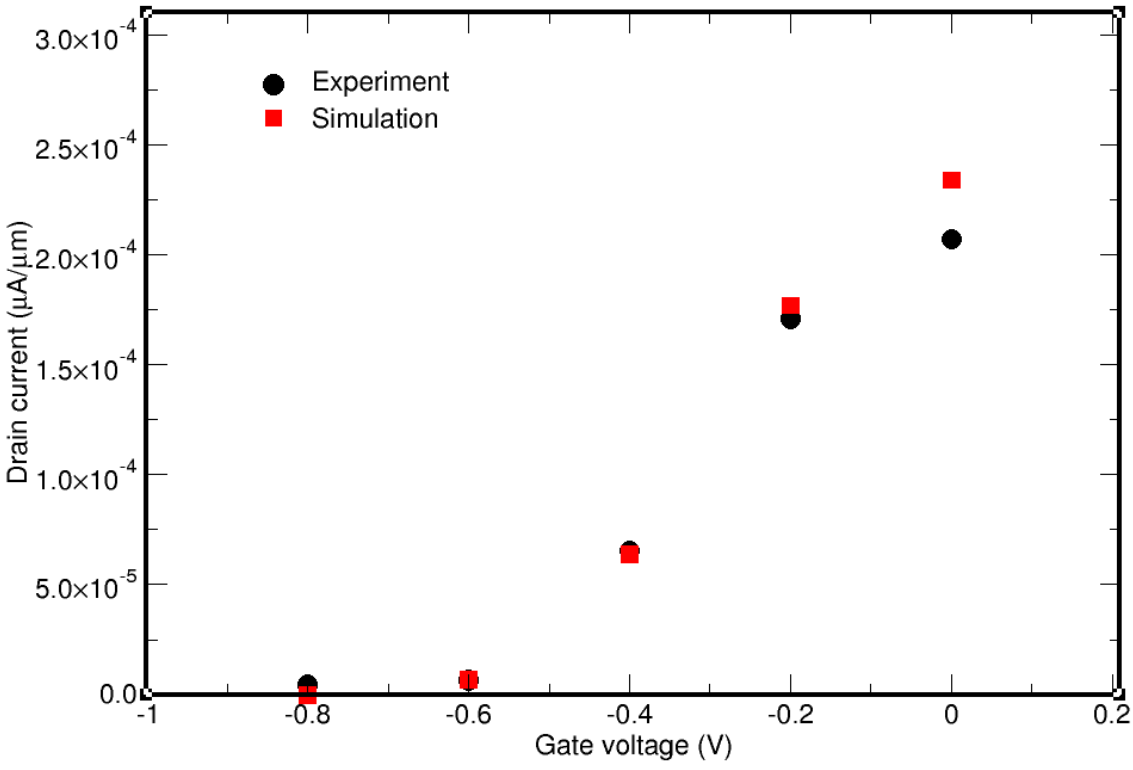

Fig. 34. Simulated DC characteristics of the HEMT modeled using 2-D TCAD compared to measured data from Device 1. The drain bias was 0.25 V in both cases.

In the ion experiments, the voltage excursion resulting from an ion event is passed on io the oscilloscope, and the corresponding drain transient current is obtained by scaling the voltage excursion by the 50 Ω termination resistance of the oscilloscope. The bias tee effectively filters out the DC component in both the experiments as well as simulation; the integrated charge is computed from a purely transient waveform. If the bias tee were absent, the DC level would factor into the integrated charge calculation. As a result, one would expect a monotonic increase in the integrated charge from depletion to accumulation as the DC level progressively increases, as shown in Fig. 35. On the other hand, one would expect an integrated charge response qualitatively similar to that observed in the experiments with the bias tee model in place. Both of these cases were confirmed in simulations, as shown in Fig. 35.

In the case without the bias tee model, the normalized integrated charge increased from depletion to accumulation. In the case with the bias tee model in place, the integrated charge trend was similar to that found in experiments. These simulations confirmed that the 2-D TCAD HEMT model functionally represented the device operation both in static (DC) and transient (single-event) modes. The next section details the mechanisms behind the observed single-event response in the experiments.

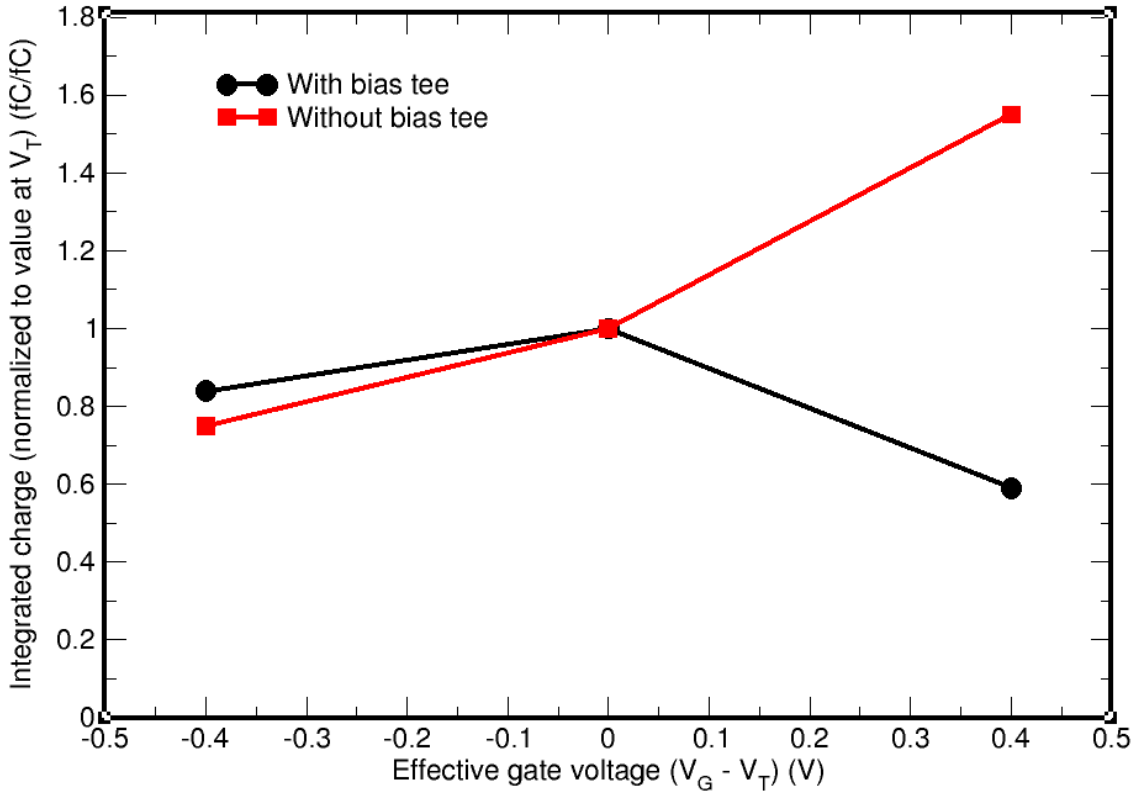

Fig. 35. 2-D TCAD simulation results of an InAlSb/InAs/AlGaSb HEMT with and without the use of bias tee

E. Mechanisms

(i) Basic charge collection mechanisms

Following a single-event strike, the radiation-generated electrons and holes move under the influence of the electric field towards the drain and source, respectively, since the drain is biased positively with respect to the source. Two charge collection mechanisms influence the InAlSb/InAs/AlGaSb HEMTs. The first is the direct collection of the radiation-generated electrons and holes at the drain and source contacts, respectively. The second type of mechanism involves charge enhancement due to source-channel barrier lowering following a single-event strike. The total integrated charge is a sum of the charges collected from each of the two mechanisms. When charge enhancement occurs, it

overwhelms the direct collection process because of the very nature of the phenomenon, i.e., there's an amplification of the charge deposited from the strike due to source injection as seen in Fig. 36. A reduction of charge enhancement would thus mean that the charge collection process would be dominated by direct collection at the drain and source contacts.

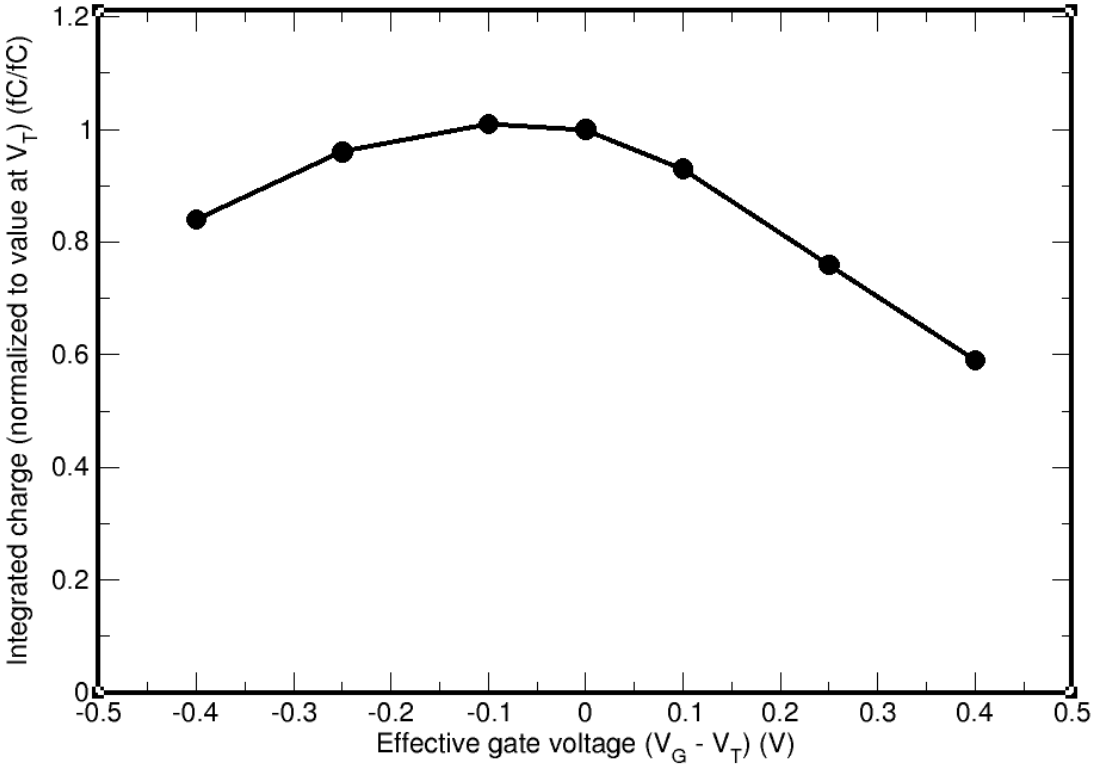

Fig. 36. Simulation results showing charge enhancement leading to increased integrated charge reaching a maximum at V_T.

The source-channel barrier lowering involves injection of charge from the source into the channel over the lowered barrier and collected at the drain [13, 63]. Therefore, the contribution to the total integrated charge from the direct collection of radiation-generated electrons at the drain can be determined by looking at the ratio of the integrated charge from the source to that from the drain. Identical integrated charges from the

source and drain transients would imply no direct contribution from the radiation-generated electrons or holes, and an absence of charge enhancement. A greater integrated charge contribution from the source transient than that from the drain transient would imply a corresponding greater net collection of radiation-generated holes (charge enhancement) at the source, since the source is biased negatively with respect to the drain.

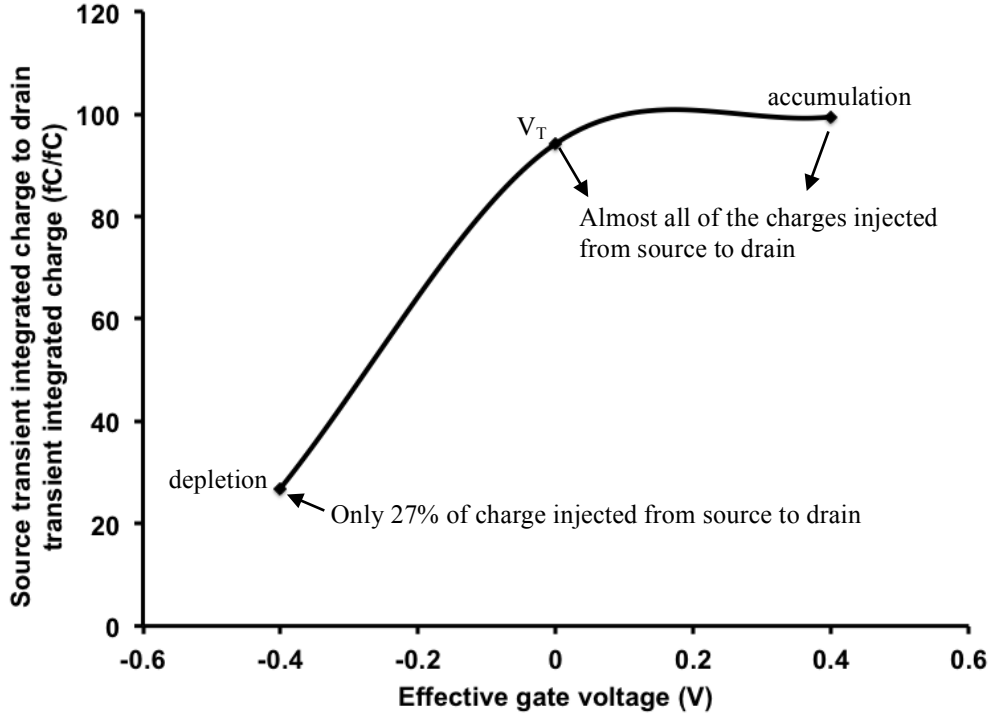

Fig. 37. Ratio of integrated charge from source transient to that from the drain transient, as seen from simulations.

Apart from the direct collection of radiation-generated holes at the source, the excess holes at the source for charge enhancement would have to originate from the buffer, following a single-event strike. However, due to the type-II band alignment, the holes cannot be transported from the buffer to the channel and reach the source, since it is energetically unfavorable for the holes to do so. The 2-D TCAD simulations show that

the third possibility is favored, where the integrated charge from the drain transient is greater than that from the source transient, as shown in Fig. 37. It is seen that 73% of the charge comes from direct collection of electrons at the drain contact in depletion. In other words, only 27% of the charge comes from the source injection at depletion, while the rest are from the direct collection of radiation-generated electrons.

The second type of charge collection mechanism involving charge enhancement occurs primarily due to the type-II band alignment of the InAlSb/InAs/AlGaSb HEMT. This alignment favors accumulation of holes in the AlGaSb buffer post-strike as seen from simulations in Fig. 38, where the hole density increases dramatically post-strike. In this figure, the "initial" and "peak of strike" refer to the simulation conditions just before the single-event strike and at 25 ps post-Gaussian peak of the strike, respectively. Figure 38 corresponds to a HEMT biased at threshold, and a drain bias of 0.25 V.

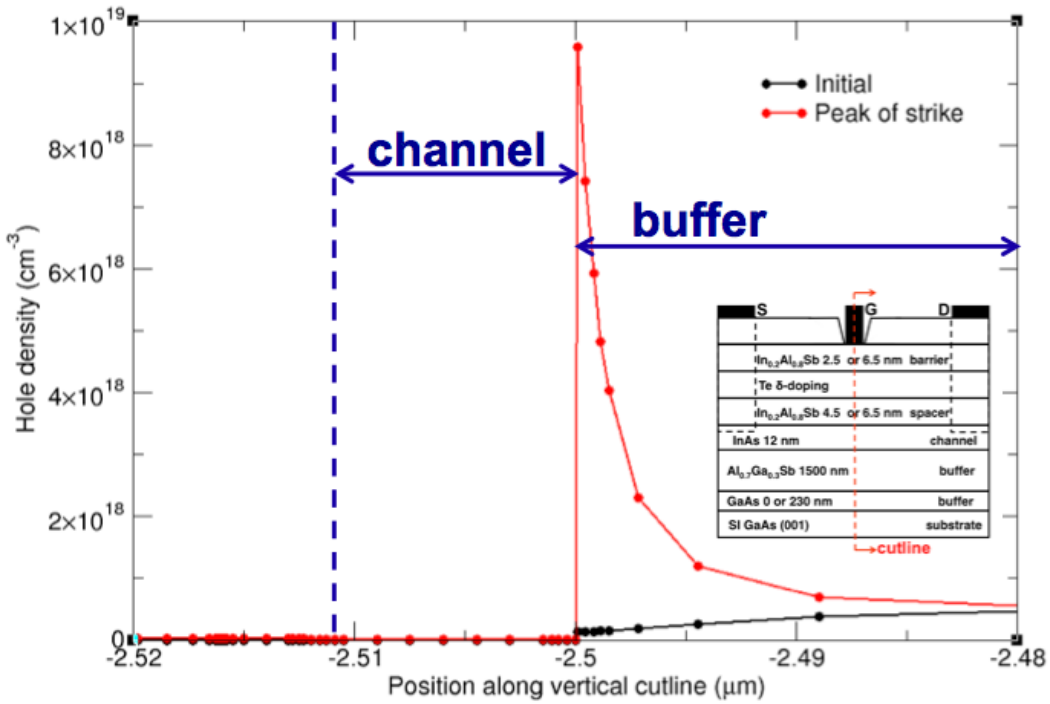

Fig. 38. Hole density in the buffer pre- and post strike, as seen in simulations. The plot is obtained from a vertical cutline through the center of the gate (along Y-Y' in Fig. 16(a) of Chapter III).

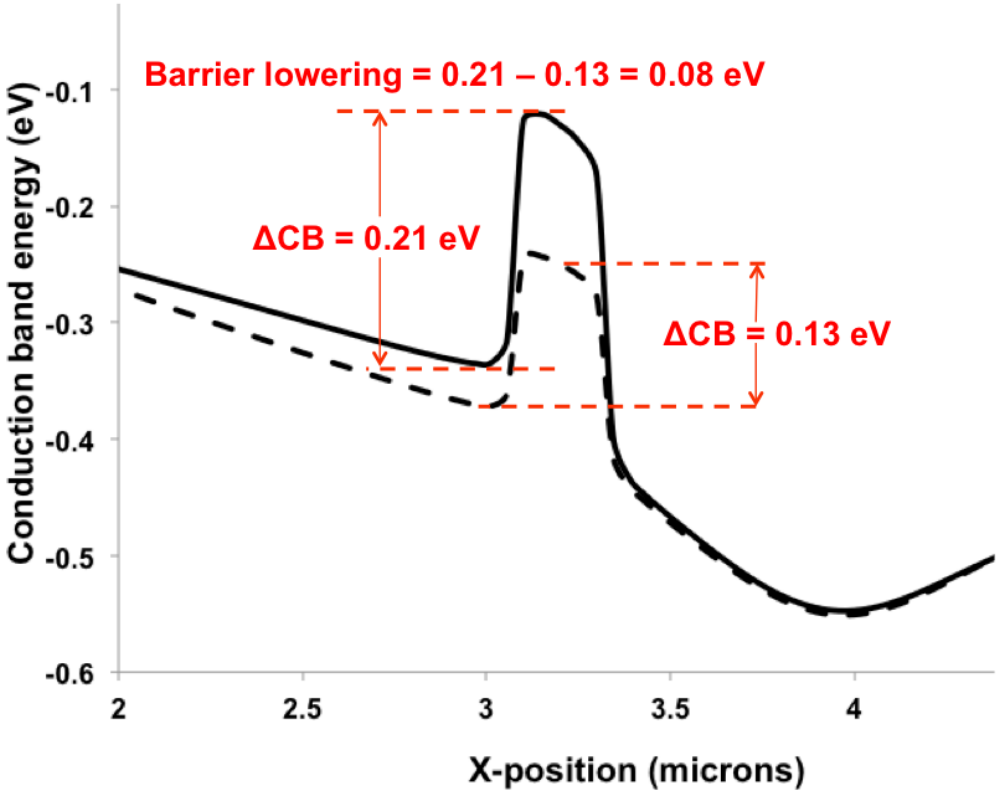

Fig. 39. The source-channel barrier lowering and corresponding charge injection, obtained from a horizontal cutline (along X-X' in Fig. 16(a) of Chapter III) through the center of the channel. The solid and dashed lines represent the initial and peak-of-strike conditions respectively.

The hole accumulation lowers the barrier between the source and the channel, thereby favoring the injection of electrons from the source into the channel over the lowered barrier, and collected at the drain terminal, as seen in Fig. 39. The change in conduction band energies between the edges of the gate and the source respectively for both "initial" and "peak of strike" cases of Fig. 38 are depicted as ΔCB in Fig. 39. The barrier lowering is defined as the difference between the changes in the respective conduction band energies, as shown in Fig. 39. As seen from Fig. 37, this mechanism is favored when the electron density in the channel is relatively higher, i.e., at threshold and in accumulation.

(ii) Bias dependence

In depletion, the channel is depleted of carriers, and the initial electron density in the channel is lower than that in threshold and accumulation by more than six orders of magnitude. The vertical gate field is greater than the corresponding field at threshold and therefore attracts more holes under the gate, resulting in relatively more barrier lowering in depletion. However, the accumulated holes do not substantially modulate the source charge injection, accounting only for 27% of the total integrated charge as seen from Fig. 37.

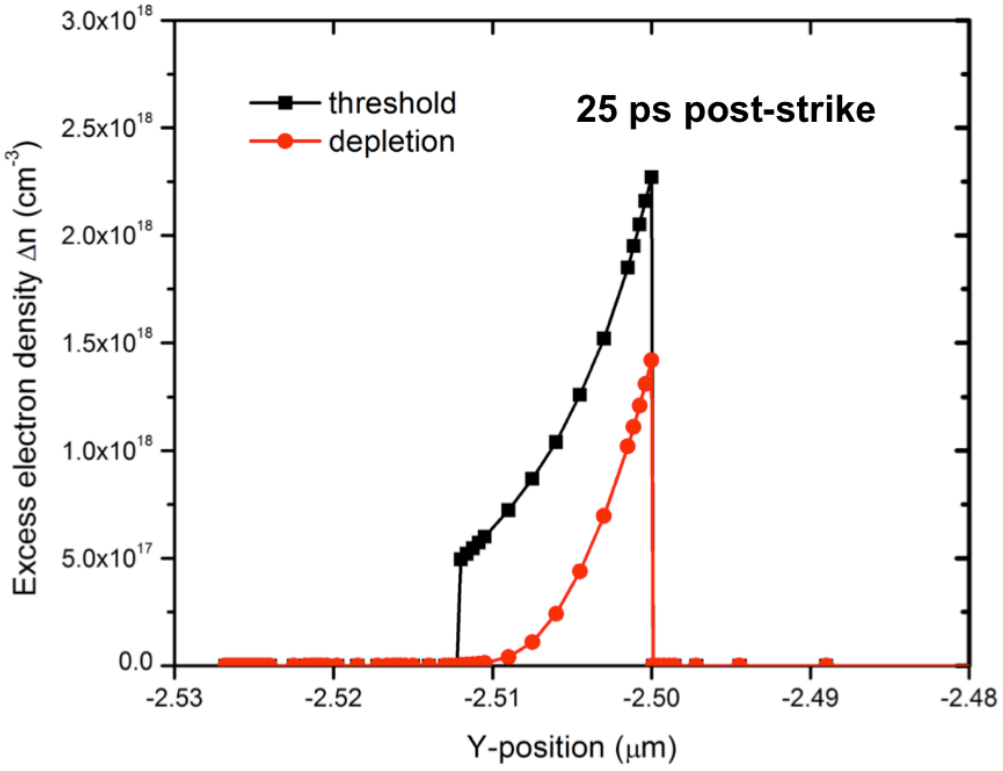

Fig. 40. Excess channel electron density obtained along a vertical cutline (along Y-Y' in Fig. 16(a) of Chapter III) through the center of the channel.

Such a relatively low amount of charge injection to an already depleted channel does not increase the net channel charge more than that at threshold, as seen in Fig. 40.

Therefore, despite the greater barrier lowering in depletion, the total collected charge in depletion is lower than that at threshold.

As the bias increases from depletion to threshold, the channel electron density and the corresponding contribution to the integrated charge from the source-channel barrier lowering increases progressively, from 27% at depletion to 94% at threshold, as seen in Fig. 37. Moving toward accumulation, almost all charge comes from source injection. Additionally, the electric field in the channel becomes more negative from threshold to accumulation, as seen in Fig. 41.

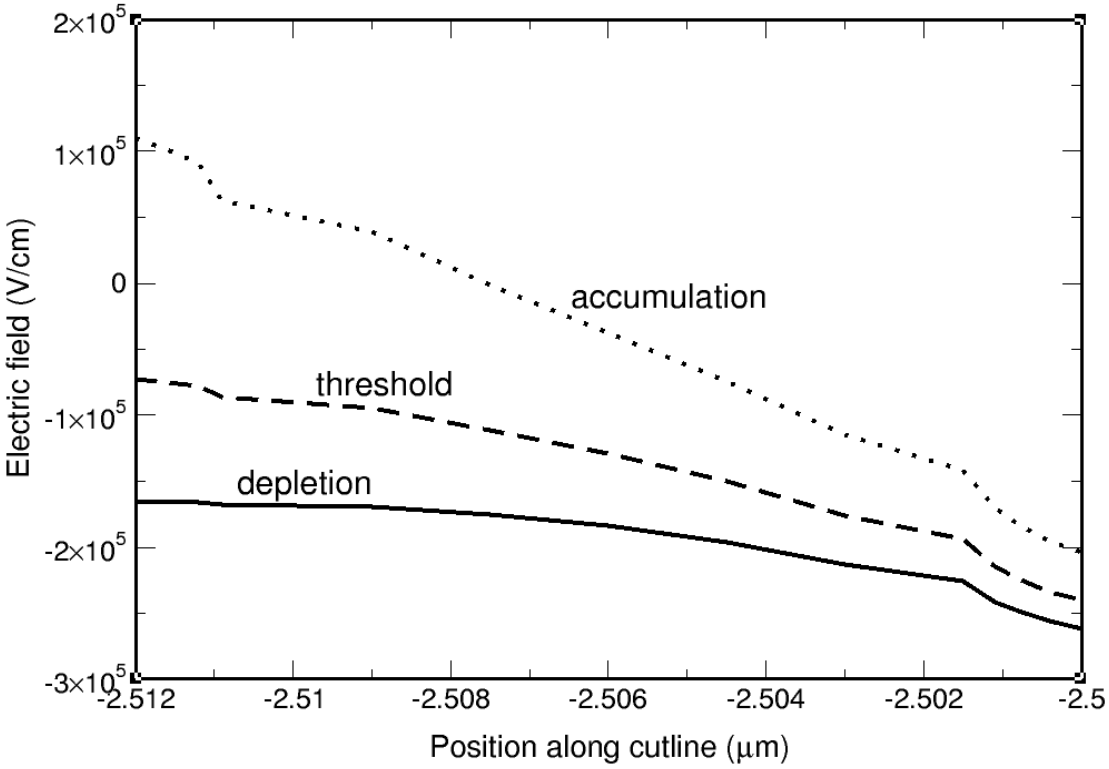

Fig. 41. Electric field in the channel for different biases, as seen from simulations. The entire x-axis represents the channel width. The plot is obtained from a vertical cutline (along Y-Y' in Fig. 16(a) of Chapter III) through the center of the gate

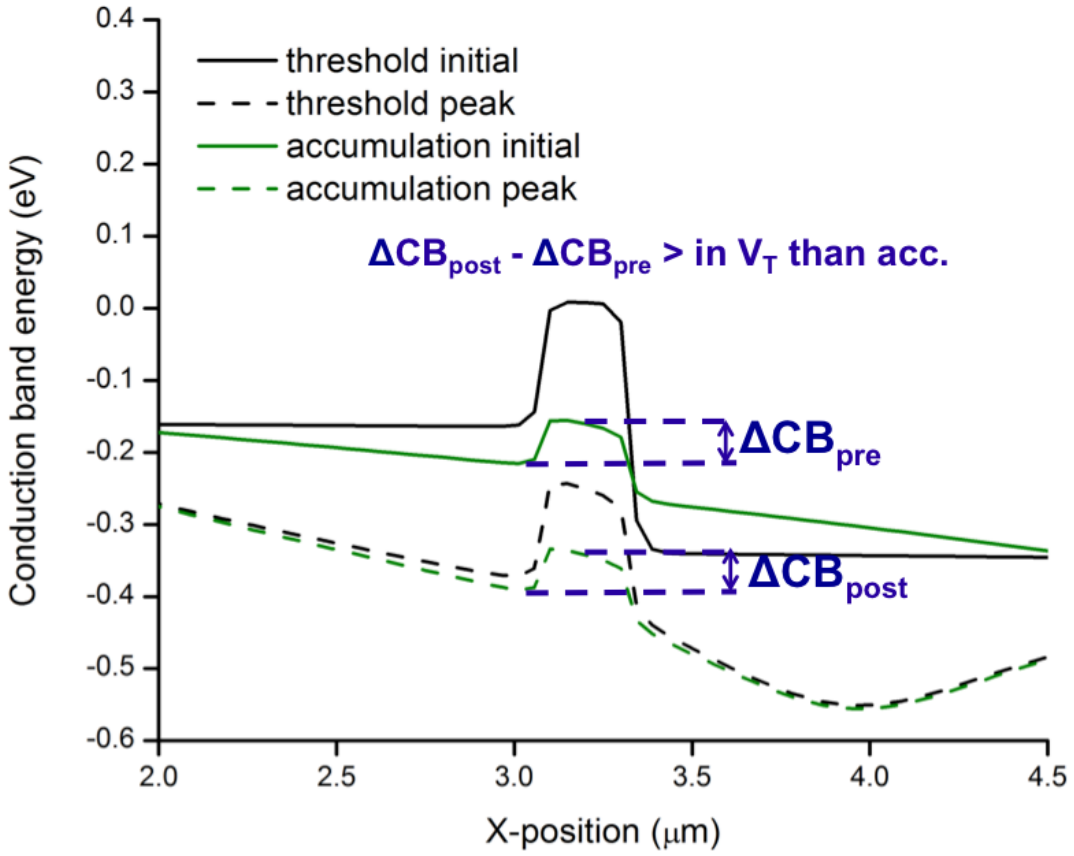

Fig. 42. Barrier lowering pre- and post-strike in threshold and accumulation, obtained from a horizontal cutline through the center of the channel (along X-X' in Fig. 16(a) of Chapter III).

Therefore, the gate attracts fewer holes and becomes more favorable for electrons in accumulation. Consequently, the potential barrier lowering between the source and channel becomes lower in accumulation than at threshold, as seen in Fig. 42, thereby lowering the corresponding integrated charge in accumulation compared to threshold.

This chapter looked at the single-event mechanisms in InAlSb/InAs/AlGaSb HEMT in detail. In particular, the prevalence of strong single-event transient sensitivity to gate bias was investigated through broadbeam experiments and simulation. Direct collection of radiation-generated electrons with minimal charge enhancement and a reversal of electric field in the channel reduced integrated charge collection at depletion and accumulation biases respectively, leading to maximum integrated charge at threshold bias. The next

chapter focuses on the effects of processing-induced threshold voltage variations on the corresponding single-event response.

CHAPTER VI

SINGLE-EVENT RESPONSE SENSITIVITY TO THREHSOLD VOLTAGE VARIATIONS IN InAlSb/InAs/AlGaSb HEMTs

A. Evolving process techniques

The previous chapter describes the strong single-event transient sensitivity to gate bias. The integrated charge peaks at threshold and dezcreases on either side of threshold, towards depletion and accumulation. Given the evolving processing techniques of InAlSb/InAs/AlGaSb HEMTs, threshold voltage variations among devices from the same die are not uncommon. This would have a direct impact on the corresponding integrated charge as seen in the previous chapter. In this chapter, the sensitivity of single-event responses to threshold voltage variations resulting from changes in device properties such as the buffer and delta-doping, and barrier and channel thicknesses are studied.

The threshold voltage V_T of any single-sided modulation-doped structure is given by [64]:

$$V_T(T) = \phi_M - \Delta E_C(T) - \frac{qN_d d_t(\frac{d_t}{2} + d_s)}{\varepsilon_0 \varepsilon_r} + \Delta E_F(T) \quad (1)$$

where Φ_M (Schottky gate workfunction), ΔE_C (conduction band offsets between the barrier and the channel), N_d (delta-doping level), d_t (thickness of the delta-doping layer), d_s (thickness of the spacer layer), and ΔE_F (change in the position of the Fermi level with respect to the conduction band minima of the InAs channel) represent the HEMT parameters. The effect of change in threshold voltage (and hence the DC characteristics) is considered because the threshold voltage represents the boundary between depletion

and accumulation of carriers in the channel, which in turn changes the drain current at a given value of gate bias, thereby impacting the corresponding single-event response.

B. Buffer doping sensitivity

The unintentional doping concentration of the AlGaSb buffer grown on a SI GaAs substrate has been shown to be strongly p-type and highly dependent on growth temperature as well as the aluminum concentration used [58, 59]. A slight change in the growth temperature can therefore affect the threshold voltage of the device. Figures 43 and 44 show the simulated DC characteristics and corresponding simulated integrated charge for three different buffer doping values – standard, and an order of magnitude lower and higher than standard. Lower and higher doping values in the buffer can shift the threshold voltage to the left or right, respectively, as seen in Eq. (1). In the simulations, the gate and drain biases were kept constant. Therefore, the changes in the threshold voltage correspond to changes in effective gate biases, which are plotted in Fig. 43. Lower and higher doping shift the device into accumulation and depletion, respectively, accounting for behavior similar to that seen in the previous section.

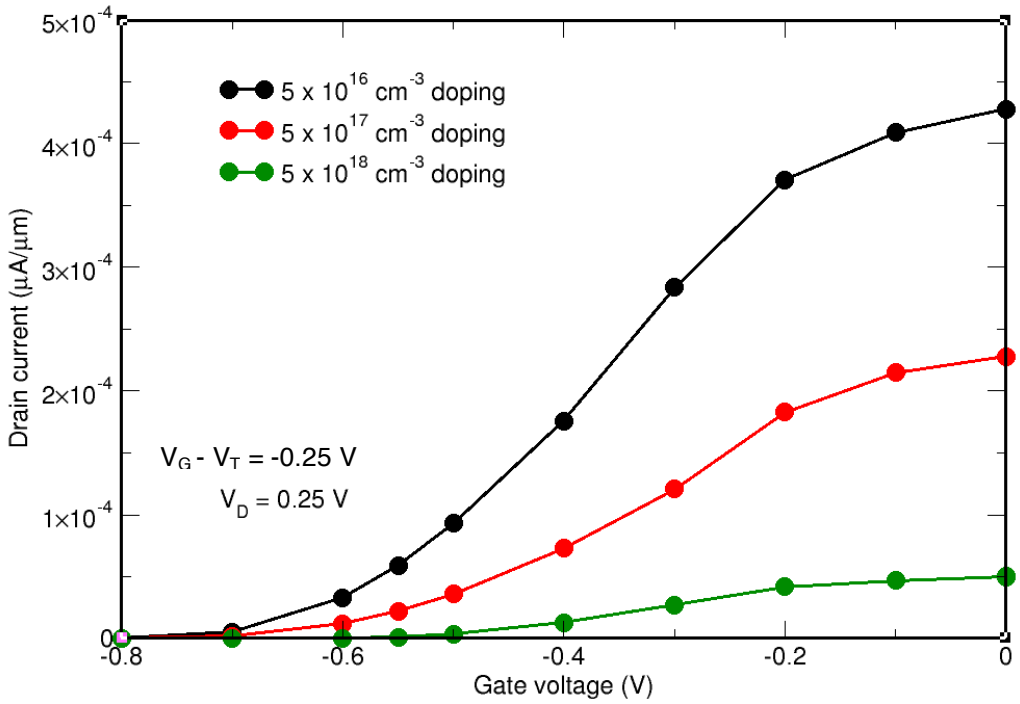

Fig. 43. Simulated DC characteristics for three different value of buffer doping.

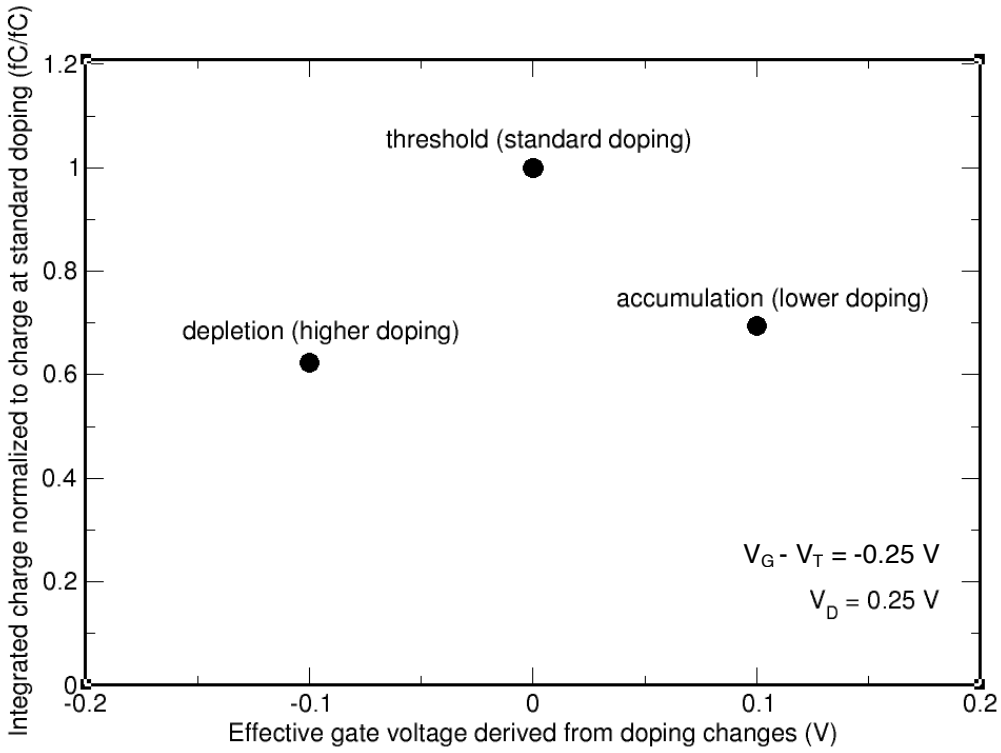

Fig. 44. Simulated integrated charge for three different buffer doping values.

C. Delta doping variation sensitivity

Equation (1) shows the direct relationship between delta-doping and V_T. As the delta-doping increases, V_T becomes more negative. This corresponds to a 18% decrease in the DC characteristics as shown in Fig. 45, for a 20% variation in delta-doping, from the standard delta-doping value of $2.5 \times 10^{18}/cm^3$ [7].

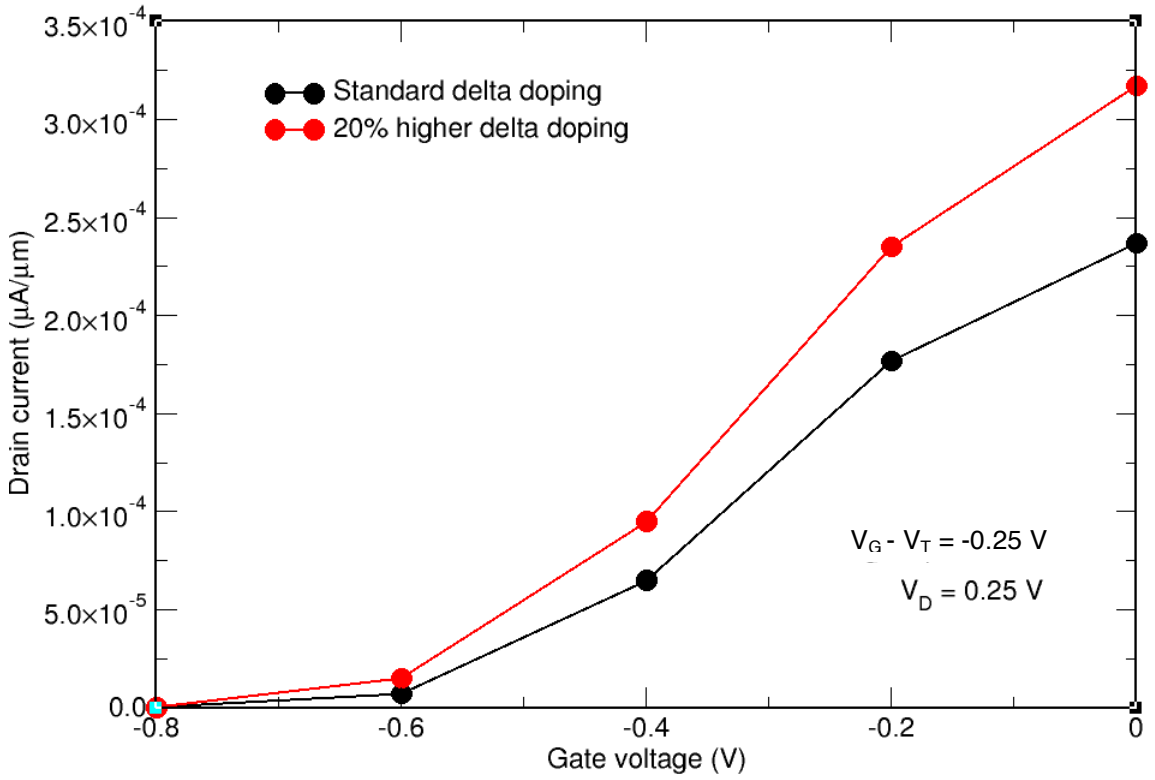

Fig. 45. Simulated DC characteristics for two cases of delta doping varying by 20%. The red data points represent the higher delta doping value.

Since the standard delta-doping corresponds to depletion in this case, the lowered threshold voltage produced by the greater delta-doping for the same gate bias represents a shift towards threshold. This is shown in Fig. 46, where the electron density in the channel is higher than that in the original case. The integrated charge is therefore higher

for the greater delta-doping case because of greater source-channel injection as seen in the previous chapter.

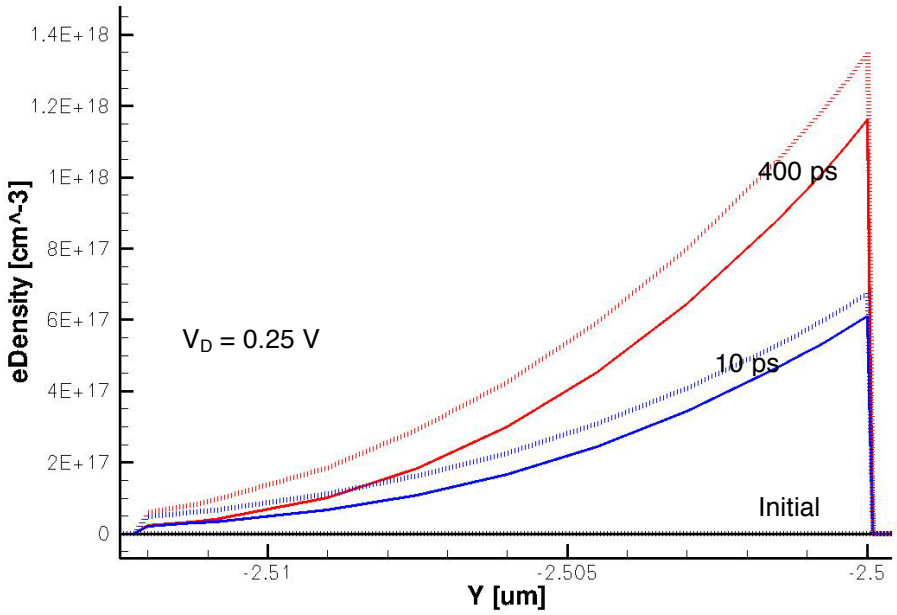

Fig. 46. Simulated vertical cross-section plot of electron densities for standard (solid lines) and 20% excess delta-doping (dotted lines) values for three time steps – initial (pre-strike), 10 ps, and 400 ps post peak of strike. The higher delta-doping value consistently has higher electron doping density for the same effective gate bias, accounting for more integrated charge.

D. Barrier thickness variation sensitivity

A variation in the barrier thickness accounts for increasing the distance between the gate and the 2DEG. From equation (1), it is evident that such an increase shifts the threshold to the left (i.e., lower value) since the vertical electric field beneath the gate decreases in case of a thicker barrier. Simulations confirm the lowered threshold voltage in case of a 50% thicker barrier as seen in the DC characteristics of Fig. 47. For a given gate bias, this represents a relatively less-depleted channel for the thicker barrier as compared to the thinner barrier.

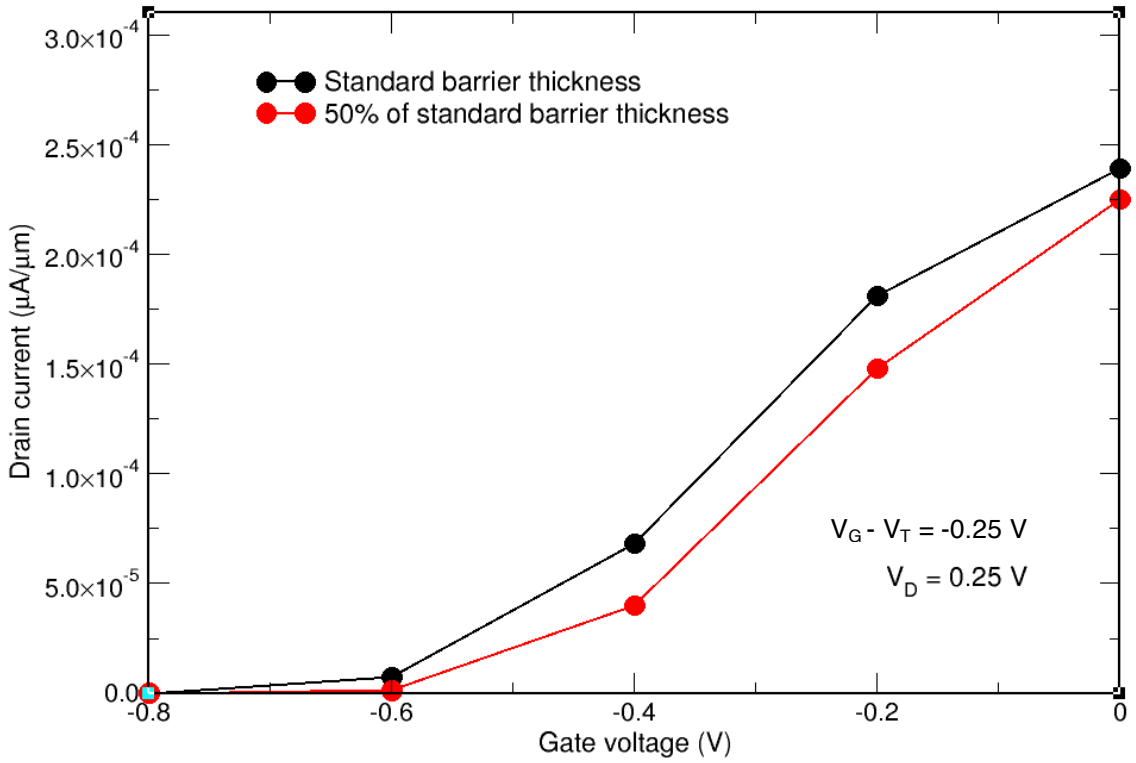

Fig. 47. Simulated DC characteristics for two values of barrier thicknesses. The red data points represent a barrier thickness 50% lower than the standard thickness of 6 nm.

The thinner and thicker barriers thus represent cases of relatively lower and higher channel electron density, respectively. Given that the gate bias corresponds to depletion for the standard barrier thickness, the lower threshold voltage value produced by the thicker barrier is representative of shifting the bias towards threshold as shown in Fig. 48, where the electron density in the channel is higher than that in the thinner barrier. Subsequently, this leads to a relatively higher integrated charge in the device with the thicker barrier as compared to the one with the thinner barrier.

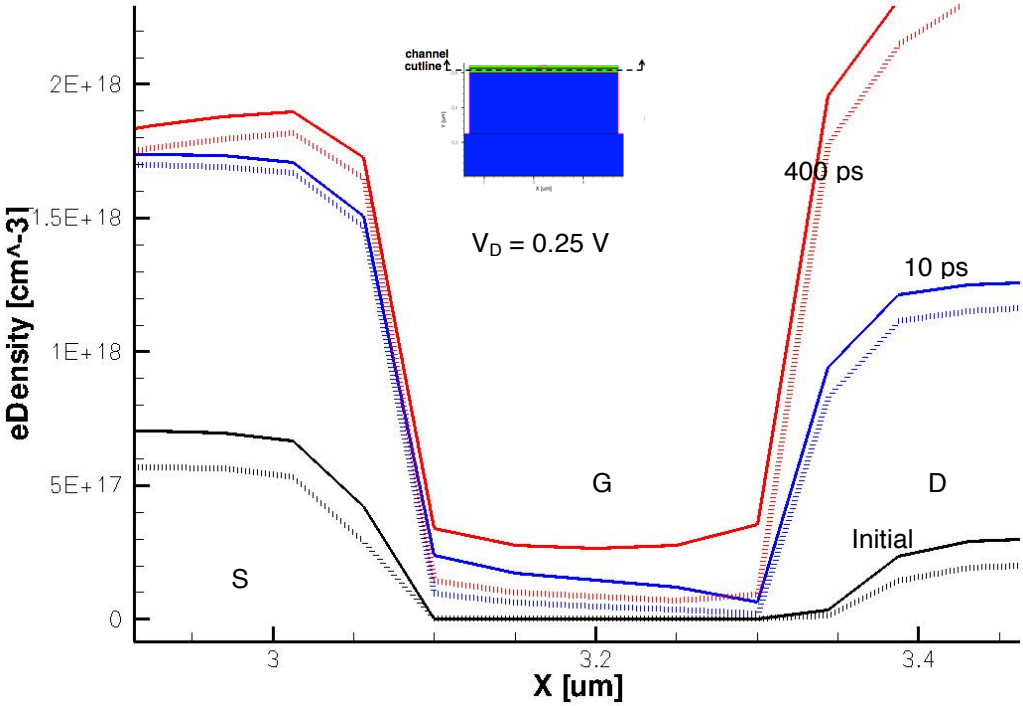

Fig. 48. Simulated horizontal cross-section plot of electron densities for standard (solid lines) and 50% lower barrier thickness (dotted lines) values for three time steps – initial (pre-strike), 10 ps, and 400 ps post peak of strike. The thinner barrier has lower electron densities at all time stamps for identical effective gate and drain biases, accounting for correspondingly lower integrated charge.

E. Channel thickness variation sensitivity

An increase in channel (InAs layer) thickness decreases the channel resistance. Additionally, it also decreases the gate control since the overall vertical electric field underneath the gate is reduced on account of the increased distance between the 2DEG and the gate. This reduction is similar to the increased barrier height case above. Figure 49 shows the DC characteristics of the HEMT for two different channel thicknesses. The thicker channel has both a relatively higher electron density as well as a lower threshold voltage as compared to the thinner channel.

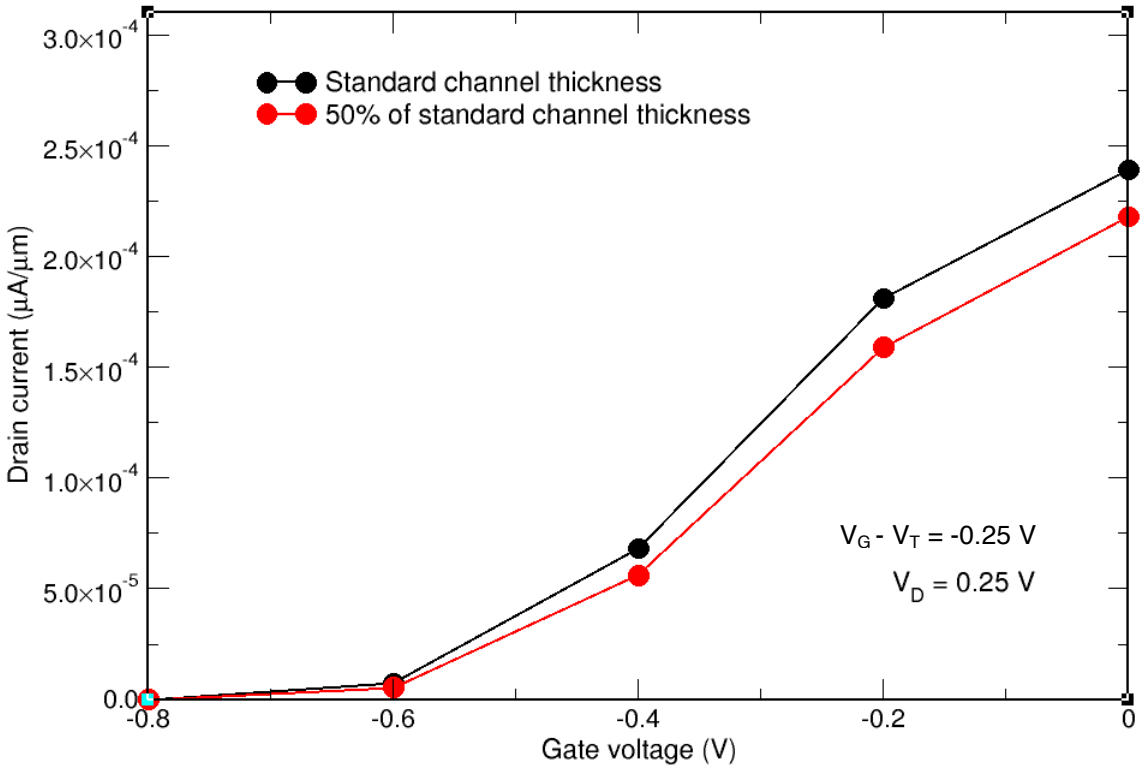

Fig. 49. Simulated DC characteristics for two values of channel thicknesses. The red data points represent a 9 nm channel and the black that of standard thickness of 12 nm.

Similar to the thicker barrier case, the device with the thicker channel is closer to threshold than depletion, compared to an identical device with a thinner channel. This subsequently leads to increased integrated charge in the device with the thicker channel as compared to that with the thinner channel.

F. Oxygen impurity sensitivity

Incorporation of oxygen as an impurity occurs during processing into the AlGaSb buffer deposited on SI GaAs of an AlSb/InAs/AlSb HEMT [18]. Since InAlSb/InAs/AlGaSb HEMTs also include an AlGaSb buffer on an SI GaAs substrate, the implications of oxygen impurity incorporation on the corresponding single-event

response were studied through 2-D TCAD simulations. Oxygen impurities in AlGaSb undergo significant structural changes upon hole capture, resulting in deep levels of trapped holes, similar to those seen in AlSb [65]. Therefore, oxygen impurities manifest themselves as deep hole traps in the AlGaSb buffer, which can cause a large decrease in threshold voltage on being occupied by holes. Deep traps are also effective SRH recombination centers and therefore, in addition to decreasing threshold voltage, their presence can directly alter the dynamics and population of carriers inside the buffer thereby directly affecting the drain transient profile. Simulations incorporating the deep traps in the AlGaSb buffer revealed that the large current drive brought on by the strong reduction in threshold voltage and the SRH recombination of electrons and holes (from the strike) at the deep trap sites suppressed the drain transient as seen in Fig. 50, leading to drastically lowered integrated charge.

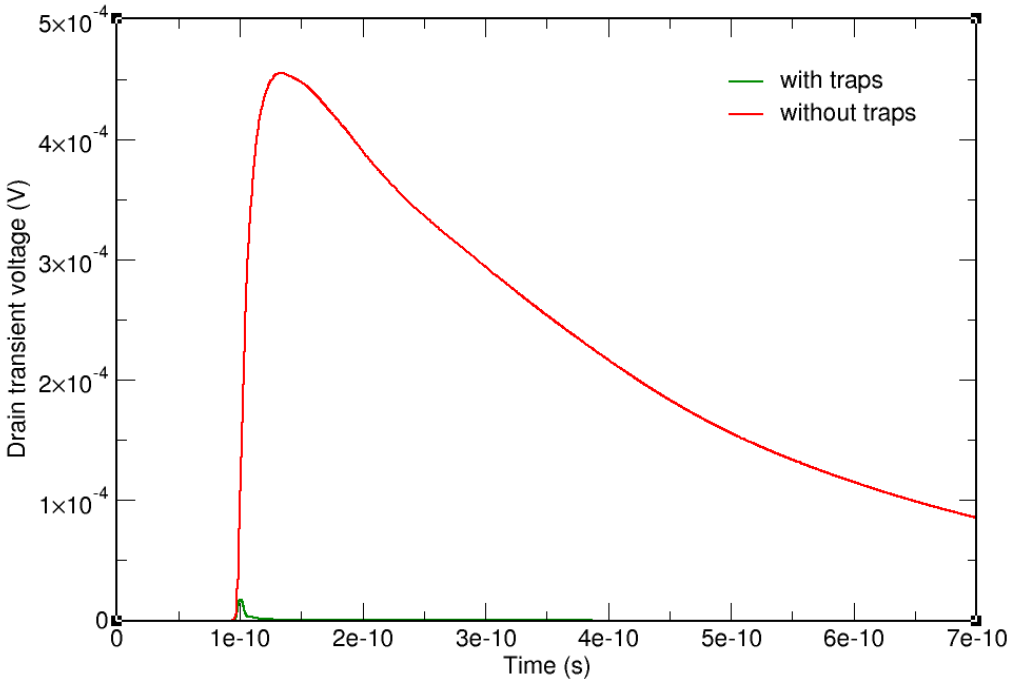

Fig. 50. Simulated drain current transients with and without the incorporation of hole traps emulating oxygen impurities in the AlGaSb buffer. A dramatically reduced drain transient results from the hole trap incorporation.

This chapter explored the effects of threshold voltage variations brought on by changes in device features and the corresponding effects on single-event response at a fixed gate and drain bias. The variations primarily result in a net charge change in the channel. Increased barrier, delta-doping, and channel thicknesses result in lowered threshold voltages and corresponding higher integrated charge for a given gate and drain bias. Given the fact that such variations in the above parameters are not uncommon in devices from the same wafer in InAlSb/InAs/AlGaSb HEMTs, these simulation results serve as an useful aid in discerning integrated charge trends for any variations encountered.

CHAPTER VII

CONCLUSIONS

This dissertation presented a detailed look into the single-event transient mechanisms in InAlSb/InAs/AlGaSb HEMTs through experiments and 2-D TCAD modeling. While these HEMTs exhibit excellent DC and RF performance similar to AlSb/InAs/AlSb HEMTs, making them attractive for potential space applications, the single-event response had not been characterized in detail in these HEMTs. Additionally, one of the key aims of the dissertation was to aid the technology development of the InAlSb/InAs/AlGaSb HEMTs. This research studied the effects of threshold voltage shifts brought about by device feature variations (such as buffer and delta-doping, and barrier and channel thicknesses), and impurity incorporation in the AlGaSb buffer, on the corresponding single-event response. The outcome of these studies could be used to understand the sensitivity of single-event response to particular device feature variations, and use them to refine the device processing. For example, the unintentional buffer doping is sensitive to growth temperature [60, 61], and therefore, changes in the temperature during processing could result in threshold voltage changes as seen in Chapter VI. This could serve as useful input to process engineers and ensure relatively tighter control of the buffer growth temperature, thereby reducing the threshold voltage variations. In turn, this would reduce the corresponding single-event response sensitivity.

Through broadbeam and microbeam experiments, it has been conclusively shown that transients can be produced by strikes in the drain pad region, resulting in single-event cross-sections greater than the active area between the source and drain. It has been

demonstrated that the single-event-induced charge collection in InAlSb/InAs/AlGaSb HEMTs depends strongly on the gate bias, peaking near threshold and decreasing toward both depletion and accumulation biases. While direct collection of radiation-generated electrons dominates when the channel is relatively depleted of carriers, a charge enhancement process resulting from source-to-channel barrier lowering dominates when the channel carrier density is relatively higher. In depletion, direct collection of radiation-induced charge dominates and results in decreased channel net charge, leading to lowered integrated charge than that at threshold. The source-channel barrier lowering increases progressively and peaks at threshold, accounting for maximum integrated charge. In accumulation, a smaller barrier lowering under the gate and an electric field reversal in the channel again results in less integrated charge than that at threshold. 2-D TCAD modeling studies reveal that decreased buffer doping, increased barrier and delta-doping, and increased channel thicknesses result in lowered threshold voltages and corresponding higher integrated charge for a given gate and drain bias. The presence of oxygen impurities has been shown to result in a large threshold voltage shift and dramatically suppress single-event transient generation.

Looking into the future, a thorough reliability characterization of the RF performance of these devices would be immensely useful. In particular, when the operating drain voltages are in the impact ionization regime, a study of defect characterization on the AC transconductance would be useful, since the absence of a hole barrier in the top InAlSb layer in this HEMT could potentially lead to issues. Finally, since these devices are potentially good candidates for use in space applications, a low-temperature study to discern the presence or absence of effects such as negative persistent photoconductivity

(NPPC) would be quite useful, both from a radiation effects as well as a reliability perspective.

REFERENCES

[1] Brian. R. Bennett, Richard Magno, J. Brad Boos, Walter Kruppa, Mario G. Ancona, "Antimonide-based compound semiconductors for electronic devices: A review," *J. Solid. State Elec.*, vol. 49, pp. 1875-1895, 2005.

[2] J. B. Boos, B. R. Bennett, W. Kruppa, D. Park, J. Mittereder, R. Bass, and M. E. Twigg, "Ohmic Contacts in AlSb/InAs High Electron Mobility Transistors for Low-Voltage Operation," *J. Vac. Sci. Technol. B,* vol. 17, pp. 1022-1027, 1999.

[3] Herbert Kroemer, "The 6.1 Å family (InAs, GaSb, AlSb) and its heterostructures: a selective review," *Physica E,* vol. 20, pp. 196-203, 2004.

[4] Gary Tuttle, Herbert Kroemer, and John H. English, "Electron concentrations and mobilities in AlSb/InAs/AlSb quantum wells," *J. Appl. Phys.,* 65(12), 1989.

[5] Chanh Nguyen, Berinder Brar, Herbert Kroemer, and John H. English, "Surface donor contribution to electron sheet concentrations in not-intentionally doped InAs-AlSb quantum wells," *App. Phys. Lett.,* 60(15), 1992.

[6] N. A. Papanicolau, B. R. Bennett, J. B. Boos, D. Park, and R. Bass, "Sb-based HEMTs with InAlSb/InAs heterojunction," *Elec. Lett.,* vol. 41, pp. 1088-1089, 2005.

[7] Brian R. Bennett, J. Brad Boos, Mario G. Ancona, N. A. Papanicolau, Graham A. Cooke, and H. Kheyrandish, "InAlSb/InAs/AlGaSb quantum well heterostructures for high-electron mobility transistors," *J. Electronic Materials,* vol.36, 2007.

[8] Brian R. Bennett, M. J. Yang, B. V. Shanabrook, J. B. Boos, and D. Park, "Modulation doping of InAs/AlSb quantum wells using remote InAs donor layers," *App. Phys. Lett.,* 72(10), pp. 1193-1195.

[9] B. D. Weaver, J. B. Boos, N. A. Papanicoloau, B. R. Bennett, D. Park, and R. Bass, "High radiation tolerance of InAs/AlSb high-electron-mobility transistors," *Appl. Phys. Lett.,* vol. 87, 2005.

[10] Jeffrey H. Warner, Dale McMorrow, Stephen Buchner, J. Brad Boos, Nicolas Roche, Philippe Paillet, Marc Gaillardin, Ewart Blackmore, Michael Trinczek, Vishwa Ramachandran, Robert A. Reed, and Ronald D. Schrimpf, "Proton- Induced Transients in GaAs and InAlSb/InAs-based FETs," presented at *IEEE Radiation and its Effects on Components and Systems 2012 Conference, submitted to Trans. Nucl. Sci.*

[11] Dale McMorrow, J. Brad Boos, Alvin R. Knudson, Stephen Buchner, Ming-Jey Yang, Brian R. Bennett, and Joseph S. Melinger, "Charge-Collection Characteristics of Low-Power Ultrahigh Speed Metamorphic AlSb/InAs High-Electron Mobility Transistors (HEMTs)," *IEEE Trans. Nucl. Sci.,* vol. 46, pp. 2662-2668, 2000.

[12] Dale McMorrow, J. Brad Boos, Alvin R. Knudson, William T. Lotshaw, Doe Park, Joseph S. Melinger, Brian R. Bennett, Alphonse Torres, Veronique Ferlet-Cavrois, Jean-Etienne Sauvestre, Claudine D'Hose, and Olivier Flament, "Transient Response of III-V Field-Effect Transistors to Heavy-Ion Radiation," *IEEE Trans. Nucl. Sci.,* vol. 51, pp. 3324-3331, 2004.

[13] S. DasGupta, D. McMorrow, R. A. Reed, R. D. Schrimpf, and J. Brad Boos, "Gate Bias Dependence of Single Event Charge Collection in AlSb/InAs HEMTs," *IEEE Trans. Nucl. Sci.,* vol. 57, pp.1856-1860, 2010.

[14] Dale McMorrow, Jeffrey Warner, Sandeepan DasGupta, Vishwa Ramachandran, J. Brad Boos, Robert Reed, Ronald Schrimpf, Philippe Paillet, Veronique Ferlet-

Cavrois, Jacques Baggio, Stephen Buchner, and Olivier Duhamel, "Novel Energy-Dependent Effects Revealed in GeV Heavy-Ion-Induced Transient Measurements of Antimony-Based III-V HEMTs," *IEEE Trans. Nucl. Sci.,* vol. 57, pp. 3358-3365, 2010.

[15] Gary Tuttle, *Ph. D. Dissertation*, University of California Santa Barbara, 1993.

[16] B. Brar, G. Nagy, J. Bergman, G. Sullivan, P. Rowell, H. K. Lin, M. Dahlstrom, C. Kadow, and M. Rodwell, "RF and DC characteristics of low-leakage InAs/AlSb HFETs," *Proc. IEEE Lester Eastman Conference on High-Performance Devices,"* 2002.

[17] P. J. Riemer, B. R. Buhrow, J. B. Hacker, J. Bergman, B. Brar, B. K. Gilbert, and E. S. Daniel, "Low-power W-band CPWG InAs/AlSb HEMT low-noise amplifier," *IEEE Microwave and Wireless Components Letters,"* vol 16, pp. 40-42, 2006.

[18] C. Chou, M. D. Lange, B. R. Bennett, J. B. Boos, J. M. Yang, N. A. Papanicolaou, C. H. Lin, L. J. Lee, P. S. Nam, A. L. Gutierrez, D. S. Farkas, R. S. Tsai, M. Wojtowicz, T. P. Chin, and A. K. Oki, "0.1 μm $In_{0.2}Al_{0.8}Sb$- InAs HEMT low-noise amplifiers for ultralow-power applications," *Proc. IEDM*, pp. 617-620, 2007.

[19] James R. Schwank, "Basic Mechanisms of Radiation Effects in the Natural Space Environment," *IEEE Nuclear Space and Radiation Effects Conference Short Course,* 1994.

[20] J. A. V. Allen, C. E. McIlwain, and G. H. Ludwig, "Radiation observations with satellite 1958," *J. Geophysical Res.*, vol. 64, no. 3, pp. 271–286, 1959.

[21] D. M. Sawyer and J. I. Vette, "AP-8 trapped proton environment for solar maximum and solar minimum," NASA National Space Science Data Center, Tech. Rep., 1976.

[22] “AE8 Trapped Electron Model,” National Space Design Center, NASA-Goddard Space Flight Center.

[23] E. G. Stassinopoulos and J. P. Raymond, “The space radiation environment for electronics,” *Proc. of the IEEE,* vol. 76, no. 11, pp. 1423–1442, 1988.

[24] F. W. Sexton, “Measurement of Single Event Phenomena in Devices and ICs,” *IEEE Nuclear Space and Radiation Effects Conference Short Course,* pp. III-1 III-55, 1992.

[25] J. H. Adams, Jr., R. Silberberg, and C. H. Tsao, "Cosmic Ray Effects on Microelectronics, Part 1: The Near.Earth Particle Environment," NRL Memorandum Report 4506, August 25, 1981.

[26] P. Meyer, R. Ramaty, and W. R. Webber, "Cosmic Rays - Astronomy With Energetic Particles," *Physics Today*, vol. 27, 1974.

[27] A. J. Tylka, J. H. Adams Jr., P. R. Boberg, B. Brownstein, W. F. Dietrich, E. O. Flueckiger, E. L. Petersen, M. A. Shea, D. F. Smart, and E. C. Smith, “CREME96: A revision of the cosmic ray effects on micro-electronics code,” *IEEE Trans. Nucl. Sci.,* vol. 44, no. 6, pp. 2150–2160, 1997.

[28] R. A. Nymmik, M. I. Panasyuk, T. I. Pervaja, and A. A. Suslov, “A model of galactic cosmic ray fluxes,” *Int. J. Radiation Applications and Instrumentation. Part D. Nucl. Tracks and Radiation Measurements*, vol. 20, no. 3, pp. 427–429, 1992.

[29] J. H. Adams, Jr, "The Natural Radiation Environment Inside a Spacecraft," *IEEE Trans. Nucl. Sci.*, vol. 29, pp. 2095, 1982.

[30] R. N. Nowlin, R. D. Schrimpf, E. W. Enlow, W. E. Combs and R. L. Pease, "Mechanisms of Ionizing-Radiation-Induced Gain Degradation in Modern Bipolar Devices," *Proc. IEEE Bipolar Circuits and Tech. Mtg.,* pp. 174.177, 1991.

[31] D. M. Fleetwood, P. S. Winokur, R. A. Reber, Jr., T. L. Meisenheimer, J. R. Schwank, M. R. Shaneyfelt, and L. C. Riewe, "Effects of oxide traps, interface traps, and 'border traps' on metal-oxide-semiconductor devices," *J. Appl. Phys.* vol. 73, pp. 5058-5074, 1993.

[32] J.R. Srour, "Displacement Damage Effects in Electronic Materials, Devices, and Integrated Circuits," *IEEE Nuclear and Space Radiation Effects Conference Short Course*, Portland, 1988.

[33] G.P. Summers, "Displacement Damage: Mechanisms and Measurements," *IEEE Nuclear Space and Radiation Effects Conference Short Course*, New Orleans, 1992.

[34] J.R. Srour and J. M. McGarrity, "Radiation Effects on Microelectronics in Space," *Proc. of the IEEE*, vol. 76, pp. 1443, 1988.

[35] Robert A. Reed, "Fundamental Mechanisms for Single-Particle Induced Soft Errors," *IEEE Nuclear Space and Radiation Effects Conference, Short Course,* 2008.

[36] K. H. G. Duh, P. C. Chao, S. M. J. Liu, P. Ho, M. Y. Kao, and J. M. Ballingall, "A super low-noise 0.1 μm T-gate InAlAs/InGaAs/InP HEMT," *IEEE Microwave Guided Wave Lett.,* pp.114-116, 1991.

[37] P. M. Smith, S. J. Liu, M. Y. Kao, P. Ho, S. C. Wang, K. H. G. Duh, S. T. Fu, and P. C. Chao, "W-band high-efficiency InP-based power HEMT with 600 GHz f_{max}," *IEEE Microwave Guided Wave Lett.,* pp.230-232, 1995.

[38] L. D. Nguyen, A. S. Brown, M. A. Thompson, and L. M. Jelloian, "50-nm self-aligned-gate pseudomorphic AlInAs/GaInAs high-electron mobility transistors," *IEEE Trans. Elec. Devices,* pp. 2007-2014, 1992.

[39] D. McMorrow, J. B. Boos, D. Park, S. Buchner, A. R. Knudson, & J. S. Melinger, "Charge-collection dynamics of InP-based high electron mobility transistors (HEMTs)," *Radiation and Its Effects on Components and Systems,* pp. 132-137, 2001.

[40] Dale McMorrow, Alvin R. Knudson, J. Brad Boos, Doe Park, and Joseph S. Melinger, "Ionization-Induced Carrier Transport in InAlAs/InGaAs High Electron Mobility Transistors," *IEEE Trans. Nucl. Sci.,* vol. 51, pp. 2857-2864, 2004.

[41] A. Bouloukou, A. Sobih, D. Kettle, J. Sly, & M. Missous, "Novel high breakdown InGaAs/InAlAs pHEMTs for radio astronomy applications," *ESA Workshop on Millimeter Wave Technology and MIN Millimiter-Wave Int. Symp.*, 2006.

[42] O. Musseau, V. Ferlet-Cavrois, J. L. Pelloie, S. Buchner, D. McMorrow, and A. B. Campbell, "Laser probing of bipolar amplification in 0.25-μm MOS/SOI transistors," *IEEE Trans. Nucl. Sci.,* vol. 47, pp. 2196–2203, 2000.

[43] V. Ferlet-Cavrois, V. Pouget, D. McMorrow, J. R. Schwank, N. Fel, F. Essely, R. S. Flores, P. Paillet, M. Gaillardin, D. Kobayashi, J. S. Melinger, O. Duhamel, P. E. Dodd, and M. R. Shaneyfelt, "Investi- gation of the propagation induced pulse broadening (PIPB) effect on single event transients in SOI and bulk inverter chains," *IEEE Trans. Nucl. Sci.,* vol. 55, pp. 2842–2853, 2008.

[44] S. DasGupta, D. McMorrow, R. A .Reed, R. D. Schrimpf, J. B. Boos, and V. Ramachandran, "Process and Contamination Effects on the Single-Event Response of AlSb/InAs HEMTs," *IEEE Trans. Nucl. Sci.,* vol. 57, pp. 3262-3266, 2010.

[45] B. D. Weaver, and E. M. Jackson, "Universal behavior in irradiated high-electron-mobility transistors," *Applied physics letters*, *80*(15), pp. 2791-2793, 2002.

[46] B. R. Bennett, B. P. Tinkham, J. B. Boos, M. D. Lange, and R. Tsai, "Materials growth for InAs high electron mobility transistors and circuits," *Journal of Vacuum Science & Technology B: Microelectronics and Nanometer Structures*, *22*(2), pp. 688-694, 2002.

[47] Joshua Bergrman, "Development of Indium Arsenide Quantum Well Circuits," *Ph. D. Dissertation,* Georgia Tech, 2004.

[48] J. B. Boos, W. Kruppa, D. Park, B. Molnar, and B. R. Bennett, "AlSb/InAs HEMT's with high transconductance and negligible kink effect," *Electron. Lett.*, vol. 32, pp.688-689, 1996.

[49] J. Brad Boos, Walter Kruppa, Brian R. Bennett, Doewon Park, Steven W. Kirchoefer, Robert Bass, and Harry B. Dietrich, "AlSb/InAs HEMTs for Low Voltage, High-Speed Applications," *IEEE Trans. Elec. Dev.,* vol. 49, pp. 1869-1875, 1998.

[50] Synopsys Inc., SDevice 2-D and 3-D TCAD device simulator.

[51] S. Adachi, "Handbook of Physical Properties of Semiconductors: III-V Compound Semiconductors".

[52] P. Hill, N. Weisse-Bernstein, L. R. Dawson, P. Dowd, and S. Krishna, S, "Activation energies for Te and Be in metamorphically grown AlSb and $In_xGa_{1-x}As$ layers," *Applied Physics Letters*, *87*(9), 2005.

[53] T. Koljonen, M. Sopanen, H. Lipsanen, and T. Tuomi, “Metalorganic vapor phase epitaxial growth of AlGaSb and AlGaAsSb using all-organometallic sources,” *Journal of crystal growth*, *169*(3), pp. 417-423, 1996.

[54] P. Y. Wang, J. F. Chen, and W, K. Chen, “Structural and electrical properties of GaSb, AlGaSb and their heterostructures grown on GaAs by metalorganic chemical vapor deposition,” *Journal of crystal growth*, *160*(3), pp. 241-249, 1996.

[55] E. T. R. Chidley, S. K. Haywood, R. E. Mallard, N. J. Mason, R. J. Nicholas, P. J. Walker, and R. J. Warburton, “GaSb heterostructures grown by MOVPE,” *Journal of Crystal Growth*, *93*(1), pp. 70-78, 1988.

[56] Ronald. S. Wagner, Jeffrey M. Bradley, Carl J. Maggiore, Jerome G. Beery, and Robert B. Hammond, “An Approach to Measure Ultrafast-Funneling-Current Transients,” *IEEE Trans. Nucl. Sci.,* vol. 33, pp. 1651-1656, 1986.

[57] Picosecond Pulse Labs, 5542-219 50 GHz bias tee model

[58] Dale McMorrow, *DTRA 6.1 Program Review*, 2009.

[59] R. Dormaier, Q. Zhang, B. Liu, Y. C. Chou, M. D. Lange, J. M. Lang, A. K. Oki, and S. E. Mohney, “Thermal Stability of Pd/Pt/Au Ohmic contacts to InAlSb/InAs heterostructures for high electron mobility transistors,” *J. Appl. Phys.,* 105, 2009.

[60] W. P. Alfred *et. al, J. Electrochem Soc.* v. 105 p. 1858, 1993.

[61] B. T. Ahlburn and A. K. Ramdas, “Spectroscopic Investigation of Acceptor States in Aluminum Antimonide,” *Phys. Rev.* vol. 187, p. 932, 1969.

[62] H. Schone, D. S. Walsh, F. W. Sexton, B. L. Doyle, P. E. Dodd, J. F. Aurand, R. S. Flores, and N. Wing. "Time-resolved ion beam induced charge collection (TRIBICC) in micro-electronics." *IEEE Trans. Nucl. Sci.,* vol. 45, pp. 2544-2549, 1998.

[63] H. Schöne, D. S. Walsh, F. W. Sexton, B. L. Doyle, P. E. Dodd, J. F. Aurand, and N. Wing. "Time-resolved ion beam induced charge collection (TRIBICC) in micro-electronics." *Nuclear Instruments and Methods in Physics Research Section B: Beam Interactions with Materials and Atoms* 158, pp. 424-431, 1999.

[64] M. B. H. Breese, E. Vittone, G. Vizkelethy, and P. J. Sellin, "A review of ion-beam induced charge microscopy," *Nucl. Instr. and Meth. B,* 264(2): 345-360, 2007.

[65] V. Ramachandran, R. A. Reed, R. D. Schrimpf, D. McMorrow, J. Brad Boos, M. P. King, E. X. Zhang, G. Vizkelethy, X. Shen, and S. T. Pantelides, "Single-event Transient Sensitivity of High Electron Mobility Transistors," *IEEE Trans. Nucl. Sci.,* vol. 59, pp. 2691-2696, 2012.

[66] Patrick Roblin and Hans Rohdin, "High-Speed Heterostructure Devices," *Cambridge University Press*, 2002.

[67] X. Shen *et. al,* "Recoverable degradation in InAs/AlSb high-electron mobility transistors: The role of hot carriers and metastable defects in AlSb," *J. Appl. Phys.,* 2010.